

# Reconstruction from Projections Based on Detection and Estimation of Objects—Parts I and II: Performance Analysis and Robustness Analysis

DAVID J. ROSSI, MEMBER, IEEE, AND ALAN S. WILLSKY, SENIOR MEMBER, IEEE

**Abstract**—The problem of reconstructing a multidimensional field from noisy, limited projection measurements is approached using an object-based stochastic field model. Objects within a cross section are characterized by a finite-dimensional set of parameters, which are estimated *directly* from limited, noisy projection measurements using maximum likelihood estimation. In Part I, the computational structure and performance of the ML estimation procedure are investigated for the problem of locating a single object in a deterministic background; simulations are also presented. In Part II, the issue of robustness to modeling errors is addressed.

## PART I PERFORMANCE ANALYSIS

### I. INTRODUCTION

THE problem of reconstructing an  $n$ -dimensional function from its  $(n - 1)$ -dimensional projections arises, typically in the context of cross-sectional imaging, in a diversity of disciplines. In the two-dimensional (2D) problem, let  $f(\mathbf{x})$  represent the value of the cross-sectional function (for example X-ray attenuation coefficient) at a point specified by the vector  $\mathbf{x} = (x_1 \ x_2)'$ . The *projection* of  $f(\mathbf{x})$  at any angle  $\theta$  is a 1D function denoted as  $g(t, \theta)$  shown in Fig. 1. For a given value of projection angle  $\theta$ , the projection evaluated at the point  $t$  is the integral

$$g(t, \theta) = \int_{-\infty}^{\infty} \int_{-\infty}^{\infty} f(\mathbf{x}) \delta(t - \mathbf{x}'\boldsymbol{\theta}) dx_1 dx_2$$

$$= \int_{\mathbf{x}'\boldsymbol{\theta}=t} f(\mathbf{x}) ds \triangleq [\mathcal{R}f](t, \theta) \quad (1)$$

along the line

$$\mathcal{L}(t, \theta) = \{\mathbf{x} : x_1 \cos \theta + x_2 \sin \theta = t\} = \{\mathbf{x} : \mathbf{x}'\boldsymbol{\theta} = t\}$$

$$\boldsymbol{\theta} \triangleq (\cos \theta \ \sin \theta)'$$

$$(t, \theta) \in Y \triangleq \{(t, \theta) : -\infty < t < \infty, 0 \leq \theta < \pi\} \quad (2)$$

as shown in Fig. 2. In (1),  $\delta(t)$  is the Dirac delta function. Equation (1) corresponds to the *Radon transformation*, which maps the 2D function  $f: R^2 \rightarrow R$  into the function on a half-

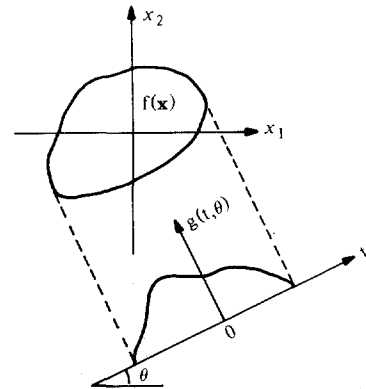


Fig. 1. Projection at angle  $\theta$ .

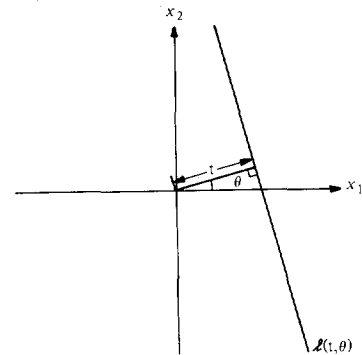


Fig. 2. Measurement geometry.

cylinder  $g: Y \rightarrow R: g(t, \theta)$  is called the Radon transform of  $f(\mathbf{x})$  [1]–[3], and is also denoted by  $[\mathcal{R}f](t, \theta)$ . The reconstruction problem, determining the function  $f$  from its projections  $g$ , is an inverse problem, since the measurements are specified by the integral equation in (1) which must be inverted to recover an estimate of the original function.

Reconstruction from projections has been employed successfully in radio astronomy, electron microscopy, medical CAT scanning, and other applications. Recently, it has been suggested that these techniques be similarly applied to a number of technologically demanding and novel applications, for example real-time monitoring of high production rate manufacturing processes, mesoscale oceanographic thermal mapping, quality control nondestructive evaluation, and “stop action” imaging of very rapidly changing media [4], [5]. Virtually all of these applications, as well as many current applications, are characterized by a limited availability of measurement data, due to:

Manuscript received August 15, 1983; revised November 18, 1983. This work was conducted at the M.I.T. Laboratory for Information and Decision Systems, and was supported by the National Science Foundation under Grant ECS-8012668.

D. J. Rossi is with Schlumberger-Doll Research, Ridgefield, CT 06877.

A. S. Willsky is with the Massachusetts Institute of Technology, Cambridge, MA 02139.

- economic constraints that limit the total number of measurement transducers—e.g., oceanographic transducers are sophisticated, low-power units that are costly to build, place, and maintain [5];
- time constraints that limit measurement quality—e.g., limited measurement time interval in “stop action” imaging of very rapid events, or in nondestructive testing of high production rate processes such as steel manufacturing [4];
- safety and operating constraints that limit the measurement quality—e.g., high temperature and/or caustic operating environments in certain process monitoring applications may limit sensor accuracy and SNR performance; in medical tomography, patient safety constrains the overall X-ray or injected radionuclide dose;
- geometrical or physical constraints that limit the view angle—e.g., in ultrasonic imaging of the heart, where bony structures limit the view angle, or in nondestructive testing of large objects;
- inaccuracy of the measurement model—the simple line integral measurement model in (1) is an idealization that does not incorporate, for example, the effects of refraction, diffraction, scattering, and polychromaticity.

It is well known, however, that when the projection measurements are limited in number or view angle, or have high noise levels, the inverse problem is ill-posed and/or has a numerically sensitive or noisy solution [1], [2], [11], [12]—that is, it is not possible to reliably produce accurate, artifact-free, and high-resolution imagery of the cross section.

In a number of applications, particularly applications where the measurement data are limited, the *ultimate* goal of processing the projection measurements is typically far more modest than obtaining high-resolution cross-sectional imagery. Rather, reconstructed imagery is an intermediate result of the overall analysis, and is itself processed (either visually or by automated or semi-automated techniques) to extract very particular information about the cross section.

In many cases, this particular information is related to objects, regions, or boundaries within the cross section. For example, in medical CAT scanning, the detection, localization, and characterization of organs and tumors is a routine step in diagnostic interpretation [6], [7]; the localization and identification of boundaries of high-contrast objects such as bone and metallic surgical clips by direct processing of projection data has also been studied [8]. Another application where object-related information is desired is oceanography; large, high-contrast thermal regions are present in many oceans (e.g., cold-core rings [5] and the Gulf stream), and oceanographic acoustic tomography has been investigated as a means of detecting and tracking these regions [5], [9]. In the area of nondestructive evaluation, tomographic techniques have also been studied for detecting and characterizing interior cracks and flaws in materials [4].

The focus of this paper is on processing projection measurements when 1) the overall goal is to extract object-related information about the cross section, and 2) limitations on the total number, SNR, or overall view angle of the projection measurements preclude the formation of high-resolution, artifact-free reconstructed imagery. In particular, an alternative to full image reconstruction is proposed and investigated that

involves processing limited, noisy projection measurements *directly*, in order to detect, locate, and characterize one or more objects within the cross section. Specifically, a stochastic, object-based field model is presented, in which objects are represented by a finite number of parameters, characterizing, say, the object location, size, boundary shape, contrast, and/or detailed internal density variations. These parameters are estimated, in the case of limited projection measurements corrupted by additive white Gaussian noise, by maximum likelihood (ML) parameter estimation [13].

While it is possible to present procedures which may be applied to cross sections containing arbitrarily complex arrangements of objects and boundaries, the focus is rather on a simpler problem, in order to lay bare the problem essentials. The specific problem considered is estimation of the *location* of a single, randomly located object situated within a known background field; problems of this type, involving detection of objects in an otherwise completely known field, have been of interest for some time in radiology [6]. Concentrating on this specific localization problem allows 1) the development of insight into the computational structure of the parameter estimation (the computation is shown to resemble one solution to the image reconstruction problem, namely the convolution back-projection (CBP) inversion formula [1]), 2) the demonstration of quantitative tools that can be utilized in critically evaluating estimator performance and robustness in a systematic manner, and 3) the establishment of a framework within which more sophisticated algorithms may be developed which take into account, for example, detailed *a priori* information about object boundary shapes, or the presence of multiple objects. One particular result obtained which demonstrates the potential utility of this approach is the identification of the minimum size of an object that can be located from given noisy projection measurements.

In developing the relatively simple localization problem, a number of simplifications are necessarily made. The robustness analysis in Part II assesses the robustness of ML object localization when applied to less idealized versions of the problem, taking into account, for example, that the real object may have a shape and density that differ from the simple assumed shape and density, or that additional, unmodeled objects may be present within the cross section. This robustness analysis, by providing insight into the sensitivity of the performance to different types of modeling errors, in turn provides intuition about potentially useful extensions or improvements in the development of more sophisticated algorithms.

In the next section, 1) a simple stochastic, object-based model for the cross section is introduced, as are models for discrete and continuous measurements, and 2) the ML object localization problem is formulated. In Section III, the error covariance of the ML location estimate is examined; both local and global errors are treated. In Sections IV and V, an example and simulations are presented which illustrate the localization of an object having a simple geometric shape.

## II. PRELIMINARY ANALYSIS

### *Cross-Sectional Model*

Suppose the cross section under investigation is represented as a known *background* function  $f_b(\mathbf{x})$ , superimposed upon

which is a single "object"—an object will be modeled as a 2D function that is an additive component of the overall cross-sectional density. The overall cross-sectional density, then, is of the form

$$f(\mathbf{x}) = f_b(\mathbf{x}) + d \cdot f_o(\mathbf{x} - \mathbf{c}) \quad (3)$$

where  $d$  represents the brightness or contrast of the object,  $f_o(\mathbf{x})$  corresponds to a unit-contrast object situated at the origin, and  $\mathbf{c} = (c_1 \ c_2)'$  denotes the object location in the plane.<sup>1</sup> Note that because the function  $f(\mathbf{x})$  depends nonlinearly (by a shift in  $\mathbf{x}$ ) on the object location, the problem of estimating  $\mathbf{c}$  from measurements of  $f(\mathbf{x})$  (or its integrals) is a nonlinear estimation problem. This is in contrast to direct image reconstruction, in which a linear estimation problem of considerably higher dimensionality is solved.

As an example of the representation in (3), consider the problem of locating a connected region  $K$  (e.g., a disk) having constant density  $d$  relative to the background. In this case, the object is a discontinuous function that equals zero everywhere except at points within the set  $K$ , where it takes on the value  $d$ . Alternatively, a circularly symmetric object of radius  $R$  and density  $d$  may be described by using a Gaussian object  $f_o(\mathbf{x}) = \exp(-\|\mathbf{x}\|^2/R^2)$ , where  $\|\mathbf{x}\|$  is the distance of the point  $\mathbf{x}$  from the origin. See [14] for a discussion of these and other continuous and discontinuous object models. In Sections IV and V, results are illustrated using as an example a discontinuous object that has a constant density on a disk.

#### Measurement Model

The cross-sectional density function  $f(\mathbf{x})$  can be observed only via limited, noisy projections. Two types of measurements are considered here, specifically, projection measurements taken over a *continuous* interval of view angle values  $\theta$  and projection measurements taken at only a finite number of *discrete* projection angles. In both cases, the measurement at angle  $\theta$  will be modeled as a convolution of the continuous 1D projection  $g(t, \theta; \mathbf{c})$  (which depends on the object location  $\mathbf{c}$ ) with a 1D measurement aperture  $h(t)$ , and corrupted by additive zero-mean white Gaussian noise,<sup>2</sup>

$$y(t, \theta) = g(t, \theta; \mathbf{c}) * h(t) + w(t, \theta) \quad (4)$$

$$\triangleq s(t, \theta; \mathbf{c}) + w(t, \theta) \quad (t, \theta) \in S \subset Y.$$

Various aperture functions may be considered, for example, a rectangular pulse aperture corresponding to strip integration, an impulsive aperture corresponding to line integration, or the sinc aperture

$$h(t) = \frac{\sin 2\pi Wt}{2\pi Wt} \quad (5)$$

corresponding to projections having a spatial bandwidth of  $W$  cycles per unit distance in the  $t$  direction. The use of a nonim-

<sup>1</sup>More generally, the object may depend on a finite number of parameters characterizing, say, its size, shape, and/or detailed boundary, and these parameters may be estimated [14].

<sup>2</sup> $y(t, \theta)$  could also be considered as a counting process with a rate that depends on  $g(t, \theta; \mathbf{c})$ . Such a model is appropriate, for example, in very low-dose X-ray problems.

pulsive measurement aperture  $h(t)$  facilitates the modeling of finite bandwidth projection measurements.

*Case 1: Continuous-View Measurements:* In the continuous-view case, measurements are taken over a total viewing angle of  $2\Delta$  centered at  $\pi/2$ , i.e., views are taken up to an angle  $\Delta$  on either side of the  $x_1$  axis (here,  $0 < \Delta \leq \pi/2$ ). The measurement set  $S$  is a subset of the half-cylinder  $Y$ , and is given by

$$S = S_\Delta \triangleq \{(t, \theta) : -\infty < t < \infty, \frac{\pi}{2} - \Delta \leq \theta < \frac{\pi}{2} + \Delta\}. \quad (6)$$

In the continuous-view case, the additive noise  $w(t, \theta)$  is a 2D zero-mean Gaussian random field on  $S_\Delta$  with covariance

$$E\{w(t, \theta)w(\tau, \phi)\} = \frac{N_o}{2} \delta(t - \tau, \theta - \phi) \quad (7)$$

where  $\delta(t, \theta)$  is a 2D impulse. The standard tomographic reconstruction problem, where (noise-free) measurements are assumed to be available at all possible projection angles, is the special case of the continuous-view measurement case where  $\Delta = \pi/2$ . This will be referred to as the *full-view* measurement case, and the case  $\Delta < \pi/2$  will be referred to as the *limited-view* measurement case.

*Case 2: Discrete-View Measurements:* In the discrete-view case, projections are measured at  $N$  angles that are uniformly spaced on the interval  $[0, \pi)$ . The measurement subset is

$$S = S_N \triangleq \{(t, \theta) : -\infty < t < \infty, \theta = \theta_j = \frac{j\pi}{N} \quad (8)$$

$$j = 0, 1, \dots, N-1\}.$$

For each view angle  $\theta_j$ , the noise process  $w(t, \theta_j)$  is a 1D zero-mean Gaussian process with covariance

$$E\{w(t, \theta_j)w(\tau, \theta_j)\} = \frac{N_o}{2} \delta(t - \tau) \quad (9)$$

and the noise at different view angles  $\theta_i$  and  $\theta_j$ ,  $i \neq j$ , is uncorrelated.

For the cross-sectional density function shown in (3), the Radon transform (1) is

$$g(t, \theta) = \int_{x'_\theta=t} f_b(\mathbf{x}) ds + d \int_{x'_\theta=t} f_o(\mathbf{x} - \mathbf{c}) ds. \quad (10)$$

Since the background function is known, the first term in (10) is known and may be subtracted from the Radon transform (this is assumed to be done for the remainder of this analysis) to leave the part due solely to the object, namely

$$g(t, \theta; \mathbf{c}) = d \int_{x'_\theta=t} f_o(\mathbf{x} - \mathbf{c}) ds. \quad (11)$$

Let  $g_o(t, \theta)$  denote the Radon transform when the object is located at the origin,

$$g_o(t, \theta) \triangleq g(t, \theta; \mathbf{0}) = d \int_{x'_\theta=t} f_o(\mathbf{x}) ds. \quad (12)$$

For an arbitrary object location  $\mathbf{c} \in C \subset R^2$ , the Radon trans-

form is, from (11) and (12),

$$g(t, \theta; \mathbf{c}) = d \int_{\mathbf{x}'\theta = t - \mathbf{c}'\theta} f_o(\mathbf{x}) ds = g_o(t - \mathbf{c}'\theta, \theta). \quad (13)$$

Equation (13) indicates the nonlinear dependence of the Radon transform  $g(t, \theta; \mathbf{c})$  on the object location. Specifically, when an object is translated from the origin to the point  $\mathbf{c}$ , its Radon transform experiences a shift in the  $t$  variable, where the magnitude of this shift,  $\mathbf{c}'\theta = c_1 \cos\theta + c_2 \sin\theta$ , depends sinusoidally on  $\theta$ .

*Example 1:* Consider a constant-density object on a disk of radius  $R$  centered at the point  $\mathbf{c}$  in the plane [see Fig. 3(a)],

$$d \cdot f_o(\mathbf{x} - \mathbf{c}) = \begin{cases} d & \text{if } \|\mathbf{x} - \mathbf{c}\| \leq R \\ 0 & \text{otherwise.} \end{cases} \quad (14)$$

For any value of  $\theta$ , the projection  $g(t, \theta; \mathbf{c})$  is a half-ellipse centered at  $t = \mathbf{c}'\theta$ ,

$$g(t, \theta; \mathbf{c}) = \begin{cases} 2d\sqrt{R^2 - (t - \mathbf{c}'\theta)^2} & \text{if } |t - \mathbf{c}'\theta| \leq R \\ 0 & \text{otherwise.} \end{cases} \quad (15)$$

This Radon transform, viewed as a function  $g: Y \rightarrow R$ , is the  $\theta$ -dependent function shown in Fig. 3(b). Note that while in this example the object  $f_o(\mathbf{x})$  is circularly symmetric, an object is generally not circularly symmetric, and consequently its Radon transform  $g_o(t, \theta)$  is  $\theta$ -dependent and nonsymmetric.

#### Maximum Likelihood Location Estimation

Given a set of continuous- or discrete-view measurements  $y(t, \theta)$ , it is desirable to estimate the object location  $\mathbf{c}$  by maximum likelihood (ML) estimation. The ML location estimate is obtained by first using the projection measurements to compute a log likelihood function  $L(\mathbf{c})$ , and then finding the 2D parameter  $\mathbf{c} \in C \subset R^2$  at which the maximum value occurs.

In the continuous-view case with a total viewing angle of  $2\Delta$ , the log likelihood function is given by [13]

$$L_{\Delta}(\mathbf{c}) = \frac{2}{N_o} \int_{\pi/2 - \Delta}^{\pi/2 + \Delta} \int_{-\infty}^{\infty} y(t, \theta) s(t, \theta; \mathbf{c}) dt d\theta - \frac{1}{N_o} \int_{\pi/2 - \Delta}^{\pi/2 + \Delta} \int_{-\infty}^{\infty} s^2(t, \theta; \mathbf{c}) dt d\theta \quad (16a)$$

and in the discrete-view case with a total of  $N$  views, it is given by

$$L_N(\mathbf{c}) = \frac{2}{N_o} \sum_{j=0}^{N-1} \int_{-\infty}^{\infty} y(t, \theta_j) s(t, \theta_j; \mathbf{c}) dt - \frac{1}{N_o} \sum_{j=0}^{N-1} \int_{-\infty}^{\infty} s^2(t, \theta_j; \mathbf{c}) dt. \quad (16b)$$

In each case, the log likelihood function is the difference between two terms, the first of which is obtained by a matched filtering operation [13] on the measurements using a filtering template  $s(t, \theta; \mathbf{c})$ . The second term compensates for the

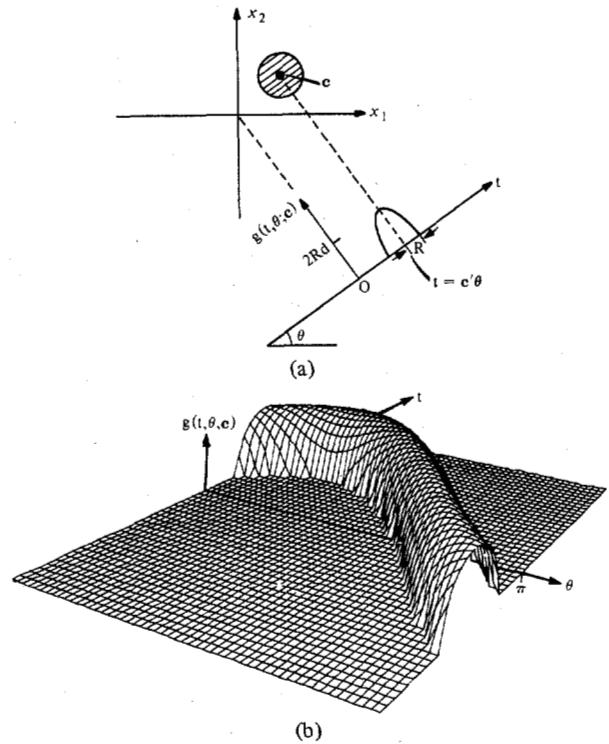


Fig. 3. (a) Projection of the disk object. (b) Radon transform of the disk object.

filtering template energy. From (4), (13), and a change of variable

$$\begin{aligned} \int_{-\infty}^{\infty} s^2(t, \theta; \mathbf{c}) dt &= \int_{-\infty}^{\infty} s^2(t - \mathbf{c}'\theta, \theta; \mathbf{0}) dt \\ &= \int_{-\infty}^{\infty} s^2(\tau, \theta; \mathbf{0}) d\tau. \end{aligned} \quad (17)$$

The final integral in (17) is  $\mathbf{c}$ -independent, so the matched filter template energy terms in (16) are constant and may be dropped, as can the first term scaling constant, leaving

$$L_{\Delta}(\mathbf{c}) = \int_{\pi/2 - \Delta}^{\pi/2 + \Delta} \int_{-\infty}^{\infty} y(t, \theta) s_o(t - \mathbf{c}'\theta, \theta) dt d\theta \quad (18a)$$

and

$$L_N(\mathbf{c}) = \sum_{j=0}^{N-1} \int_{-\infty}^{\infty} y(t, \theta_j) s_o(t - \mathbf{c}'\theta_j, \theta_j) dt \quad (18b)$$

where  $s_o(t, \theta) \triangleq s(t, \theta; \mathbf{0}) = g_o(t, \theta) * h(t)$ .

In summary, the ML estimate for the object location is determined by computing the log likelihood function in (18), and determining the value of the two-dimensional parameter  $\mathbf{c} \in C$  at which the peak of the log likelihood function occurs,

$$\hat{\mathbf{c}}_{\text{ML}} = \begin{cases} \operatorname{argmax}_{\mathbf{c} \in C} L_{\Delta}(\mathbf{c}) & \text{in the continuous-view case} \\ \operatorname{argmax}_{\mathbf{c} \in C} L_N(\mathbf{c}) & \text{in the discrete-view case.} \end{cases} \quad (19)$$

### Remarks

The convolution back-projection (CBP) inversion formula [1]-[3] is one solution to the integral equation in (1); it assumes the availability of noise-free full-view measurements and is given by

$$\begin{aligned}\hat{f}(\mathbf{x}) &= \int_0^\pi \int_{-\infty}^{\infty} g(t, \theta) v(t - \mathbf{x}'\boldsymbol{\theta}, \theta) dt d\theta \\ &= \int_0^\pi q(\mathbf{x}'\boldsymbol{\theta}, \theta) d\theta \triangleq [Bq](\mathbf{x}).\end{aligned}\quad (20)$$

This mapping of  $g \rightarrow \hat{f}$  is referred to as a convolution back-projection operation. For perfect reconstruction from full-view noise-free projections, the convolving kernel  $v(t, \theta)$  is  $\theta$ -independent, and its Fourier transform with respect to  $t$  satisfies  $V(\omega) = |\omega|$  [1], [2]. The so-called *back-projection* operator (the integral with respect to  $\theta$ ) maps the function  $q: Y \rightarrow R$  into the 2D function  $\hat{f}: R^2 \rightarrow R$ ; the latter function  $\hat{f}(\mathbf{x})$  is called the back-projection of  $q$  and is denoted by  $[Bq](\mathbf{x})$  [3].

Consider the case of full-view measurements ( $\Delta = \pi/2$ ), and notice the similarity between the log likelihood function in (18a) and the convolution back-projection inversion formula in (20). In (20), the noise-free projection measurements  $g(t, \theta)$  are used to determine a 2D reconstruction  $\hat{f}(\mathbf{x})$  by convolution back-projection with a  $\theta$ -independent convolving kernel  $v(t)$ . In (18a) with  $\Delta = \pi/2$ , the noisy projection measurements  $y(t, \theta)$  are used to determine a 2D log likelihood function by convolution back-projection with a generally  $\theta$ -dependent and nonsymmetric convolving kernel  $s_0(t, \theta)$ .

Note that although (18a) may be interpreted as a CBP, the resulting log likelihood function is *not* interpreted as a reconstructed image because the convolving kernel is not chosen with direct image reconstruction in mind. Rather, the convolving kernel  $s_0(t, \theta)$  is specified in the solution to the problem of ML estimation of the object location from noisy projection data.

In the limited-view case ( $\Delta < \pi/2$ ), and in the discrete-view case, the log likelihood function in (18) still has the same general form as the CBP operation in (20), except that the integral with respect to  $\theta$  for  $\theta \in [0, \pi)$  (i.e., the back-projection operation) is replaced by either an integral with respect to  $\theta$  for  $\theta \in [\pi/2 - \Delta, \pi/2 + \Delta)$  or by an  $N$ -point sum over  $\theta_j$ . These expressions resemble those associated with *approximate convolution back-projection reconstruction algorithms* [3]. These are practical implementations of the reconstruction formula in (20) that are used to compute approximate reconstructed images when measurements are available only on some subset of the full measurement set  $Y$ . The distinction between reconstructing an image using (20) and evaluating a log likelihood function using (18) still applies.

In terms of computational complexity, direct image reconstruction and log likelihood function evaluation both involve the determination of a 2D function whose value at any point is given by an integral or sum of weighted projection data. Consequently, both procedures require the same amount of computation for a given set of measurements. If the overall goal of the signal processing is to locate an object within a cross section, however, the task is completed when the log

likelihood function peak is found. In contrast, when a reconstructed image is formed, further image processing (e.g., 2D prewhitening and matched filtering) is required if the location of the object is to be determined.

Thus far, a parametric object-based field model has been put forth and the problem of ML estimation of object location using noisy projection measurements has been formulated. Two performance-related questions arise. 1) If the actual cross section satisfies the modeling assumptions exactly, how well can the object parameters be estimated from noisy projection data? 2) Modeling errors inevitably exist; when the model is an inaccurate representation of the actual cross section, how well can the object parameters be estimated?

The latter question is addressed in the robustness analysis of Part II. In the remainder of Part I, it is assumed that no modeling inaccuracies exist, and the former issue is investigated. The overall object location estimate error covariance, characterized by both local and global contributions, is analyzed in Section III. In this development, algorithmic or implementation issues such as efficient procedures for locating the log likelihood function peak are not discussed; instead, issues of how well one can do assuming that the ML estimation procedures can be carried out exactly will serve as the focus. In Sections IV and V, the error covariance is evaluated and computer simulations are presented for the constant-density disk object of Example 1.

### III. PERFORMANCE ANALYSIS

The maximum likelihood estimate for the location of an object in the cross section is obtained from projection measurements by first performing a CBP operation to obtain the 2D log likelihood function shown in (18), and then finding the point  $c \in C$  at which the maximum occurs. As suggested by the similarity between (18a) and (18b), the calculation of the log likelihood function for the continuous- and discrete-view measurement cases is very similar, and the general concepts involved in the continuous-view performance analysis carry over directly to the discrete-view case, although the details of the analyses differ [14]. Due to the similarity in the calculations, only the continuous-view computations will be detailed here.

Because the measurements  $y(t, \theta)$  are noisy, the location log likelihood function is a 2D random field. The point  $\hat{c}_{ML} \in C$  that maximizes this random field is a 2D random variable; in this performance analysis the second moment of this 2D random variable is characterized. First, to see how the log likelihood function depends on the measurement noise, let  $c_a$  denote the actual object location within the cross section, and substitute (4) into (18a).

$$\begin{aligned}\bar{L}_\Delta(\mathbf{c}, \mathbf{c}_a) &= \int_{\pi/2 - \Delta}^{\pi/2 + \Delta} \int_{-\infty}^{\infty} s(t, \theta; \mathbf{c}_a) s(t, \theta; \mathbf{c}) dt d\theta \\ &\quad + \int_{\pi/2 - \Delta}^{\pi/2 + \Delta} \int_{-\infty}^{\infty} w(t, \theta) s(t, \theta; \mathbf{c}) dt d\theta \\ &\triangleq \bar{a}_\Delta(\mathbf{c}, \mathbf{c}_a) + n_\Delta(\mathbf{c}).\end{aligned}\quad (21)$$

The log likelihood function is the sum of two terms,  $\bar{a}_\Delta(\mathbf{c}, \mathbf{c}_a)$ , the expected value of the log likelihood function, which is a

2D deterministic function known as the *generalized ambiguity function* [17], and  $n_{\Delta}(\mathbf{c})$ , a 2D zero-mean correlated random field with covariance

$$E\{n_{\Delta}(\mathbf{c}) n_{\Delta}(\tilde{\mathbf{c}})\} = \frac{N_o}{2} \bar{a}_{\Delta}(\mathbf{c}, \tilde{\mathbf{c}}). \tag{22}$$

The ambiguity function, since it enters both the deterministic and random components of the log likelihood function, plays a key role in the analysis of estimation performance in the problem at hand, as it does in radar and sonar applications in the analysis of estimation accuracy, ambiguity, and resolution [17].

Because  $s(t, \theta; \mathbf{c})$  depends on  $\mathbf{c}$  only by a shift in the  $t$  variable, the ambiguity function may be shown by a change of variable to depend on its two arguments only through their difference. That is, the ambiguity function at any given point  $\mathbf{c}$  depends only on the position of that point relative to the actual object location  $\mathbf{c}_a$ . Consequently, the noise  $n_{\Delta}(\mathbf{c})$  is stationary; for simplicity, the following notation for the ambiguity and log likelihood functions will be used.

$$\begin{aligned} a_{\Delta}(\boldsymbol{\epsilon}) &\triangleq \bar{a}_{\Delta}(\mathbf{c}, \mathbf{c}_a) \\ L_{\Delta}(\boldsymbol{\epsilon}) &\triangleq \bar{L}_{\Delta}(\mathbf{c}, \mathbf{c}_a) \quad \boldsymbol{\epsilon} \triangleq \mathbf{c} - \mathbf{c}_a. \end{aligned} \tag{23}$$

*Estimation Error Covariance*

At this point, the statistical accuracy of the location estimate  $\hat{\mathbf{c}}_{ML}$  will be investigated by considering  $\Lambda_e$ , the  $2 \times 2$  error covariance matrix for the location estimate,

$$\Lambda_e = E\{\mathbf{e} \mathbf{e}'\} \quad \mathbf{e} \triangleq \hat{\mathbf{c}}_{ML} - \mathbf{c}_a. \tag{24}$$

One error analysis technique useful in nonlinear ML estimation problems is to write the error covariance as a linear combination of conditional error covariances, where each term is conditioned on the event that the estimate falls into a certain subset of the overall parameter space [13]. This approach is attractive because in many cases approximate conditional error covariances may be determined quite easily if the overall parameter space is partitioned judiciously.

To apply this technique, the set of possible parameter values  $C$  is partitioned into  $M$  nonoverlapping regions  $C_0, C_1, \dots, C_{M-1}$  (for example, rectangular subsets of the plane). Letting  $E_j$  denote the event when the peak of the log likelihood function lies in region  $C_j$ , the error covariance may be expressed as

$$\Lambda_e = \sum_{j=0}^{M-1} \Lambda_j p_j \quad p_j \triangleq \text{Prob}\{E_j\} \tag{25}$$

where  $\Lambda_j$  denotes the estimate error covariance conditioned on  $E_j$ .

Two approximations are made at this time in order to simplify the analysis and provide an approximate expression for the error covariance  $\Lambda_e$ . As will be evident, the validity of these assumptions depends upon the choice of the  $C_j$ . In Section IV, a detailed example is provided which includes a discussion of how one can deduce the appropriate size for the  $C_j$  from knowledge of the ambiguity function.

1) Let  $\{\gamma_j; \gamma_j \in C_j, j = 0, 1, \dots, M-1\}$  be a set of  $M$  points (with respect to a coordinate system centered at  $\mathbf{c}_a$ ), and for simplicity, assume that  $\gamma_0 = \mathbf{c}_a \in C_0$ . Let  $L_j \triangleq L_{\Delta}(\gamma_j)$ , that is,

$L_j$  is a random variable defined to be the log likelihood function in (23) evaluated at the point  $\gamma_j$ . Since the additive measurement noise  $w(t, \theta)$  in (4) is Gaussian, the random vector  $L = (L_0, L_1, \dots, L_{M-1})'$  is Gaussian, with density  $p(L)$  and moments

$$\begin{aligned} E\{L_j\} &= a_{\Delta}(\gamma_j) \\ E\{(L_i - E\{L_i\})(L_j - E\{L_j\})\} &= \frac{N_o}{2} a_{\Delta}(\gamma_i - \gamma_j). \end{aligned} \tag{26}$$

The first simplification which is made is to approximate the log likelihood function  $L_{\Delta}(\boldsymbol{\epsilon})$  as being constant on each of the  $M$  regions, taking on the value  $L_j$  at all points in the region  $C_j, j = 0, 1, \dots, M-1$ . For this approximation to be good, the regions  $C_j$  should be sufficiently small in size so that random variables  $L_{\Delta}(\gamma')$  and  $L_{\Delta}(\gamma'')$  are highly correlated for any two points  $\gamma'$  and  $\gamma''$  in  $C_j$ ; this ensures that the value  $L_j$  at a representative point  $\gamma_j$  is indicative of the log likelihood function value over the entire region  $C_j$ . When  $L_{\Delta}(\mathbf{c})$  is thus approximated as being piecewise-constant, the computation of the probabilities  $p_j$  is simplified,

$$\begin{aligned} p_j &= \text{Prob}\{L_j > L_i, \forall i \neq j\} \\ &= \int_{-\infty}^{\infty} \left[ \int_{-\infty}^{L_j} \dots \int_{-\infty}^{L_j} p(L) dL_0 \dots dL_{M-1} \right] dL_j. \end{aligned} \tag{27}$$

In practice, the probabilities  $p_j$  are computationally intensive to determine when the log likelihood function values  $L_j$  are correlated, although some work on bounds is available [18]. In the case of uncorrelated  $L_j$ , bounds such as the union bound [13] are more easily obtained (approximately uncorrelated  $L_j$  arise when the regions  $C_j$  are large in size).

2) The exact expression for the conditional error covariance  $\Lambda_j$  in (25) is given by

$$\begin{aligned} \Lambda_j &= \iint_{C_j} (\hat{\mathbf{c}} - \gamma_0)(\hat{\mathbf{c}} - \gamma_0)' p(\hat{\mathbf{c}}|E_j) d\hat{c}_1 d\hat{c}_2 \\ &= \iint_{C_j} [(\hat{\mathbf{c}} - \gamma_j) + (\gamma_j - \gamma_0)][(\hat{\mathbf{c}} - \gamma_j) + (\gamma_j - \gamma_0)]' \\ &\quad \cdot p(\hat{\mathbf{c}}|E_j) d\hat{c}_1 d\hat{c}_2. \end{aligned} \tag{28}$$

If  $\gamma_j$  is a representative point in  $C_j$  (e.g., the centroid), then conditioned on the event  $E_j, j \neq 0$  (i.e., the event that the log likelihood function peak  $\hat{\mathbf{c}}$  lies in an incorrect region  $C_j$ ), the magnitude of  $\gamma_j - \gamma_0$  (between regions) is much larger than the magnitude of  $\hat{\mathbf{c}} - \gamma_j$  (within a region), and the conditional error covariance may be approximately written as

$$\Lambda_j \approx (\gamma_j - \gamma_0)(\gamma_j - \gamma_0)' \quad j \neq 0. \tag{29}$$

Using the approximation in (29), the error covariance in (25) may be written as

$$\Lambda_e = \begin{bmatrix} \sigma_{11}^2 & \sigma_{12}^2 \\ \sigma_{21}^2 & \sigma_{22}^2 \end{bmatrix} = \Lambda_0 p_0 + \sum_{j=1}^{M-1} (\gamma_j - \gamma_0)(\gamma_j - \gamma_0)' p_j. \tag{30}$$

In (30),  $\Lambda_0$  is the error covariance conditioned on the event that the peak of the log likelihood function lies in  $C_0$ , the region containing the true location point. If the region  $C_0$  is

small enough so that all of its points are close to the true object location  $\mathbf{c}_a$ , the Cramer-Rao bound [13] provides an accurate estimate of the covariance matrix  $\mathbf{\Lambda}_0$ , and in particular, of its diagonal components. Specifically,

$$[\mathbf{\Lambda}_0]_{ii} \geq [\mathbf{J}^{-1}]_{ii} \quad i \in \{1, 2\} \quad (31)$$

where  $\mathbf{J}$  is the  $2 \times 2$  Fisher's information matrix

$$[\mathbf{J}]_{ik} = -E \left\{ \frac{\partial^2 L_{\Delta}(\boldsymbol{\epsilon})}{\partial \epsilon_i \partial \epsilon_k} \right\} \quad i, k \in \{1, 2\} \quad (32)$$

and  $L_{\Delta}(\boldsymbol{\epsilon})$  is the log likelihood function in (23). By taking derivatives of (21), (32) may be written in terms of the ambiguity function as

$$[\mathbf{J}]_{ik} = -\frac{2}{N_o} \left[ \frac{\partial^2 a(\boldsymbol{\epsilon})}{\partial \epsilon_i \partial \epsilon_k} \right]_{\boldsymbol{\epsilon}=0} \triangleq -\frac{2}{N_o} \beta_{ik} \quad i, k \in \{1, 2\}. \quad (33)$$

When the object location estimate  $\hat{\mathbf{c}}_{ML}$  lies in the vicinity of the true location  $\mathbf{c}_a$ , then the estimate error variance is characterized in terms of  $\beta_{ik}$ , the second partial derivative of the ambiguity function evaluated at the origin.

In practice, evaluation of  $\beta_{ik}$  by taking two derivatives of the ambiguity function is tedious, particularly for a discontinuous object  $f_o(\mathbf{x})$ , since both the integrand and the limits of integration with respect to  $t$  in (21) depend on  $\boldsymbol{\epsilon}$ . The following analysis makes use of frequency domain analysis of the critical operations of interest in tomography (the Radon transform, convolution, and the back-projection) to develop an expression for  $\beta_{ik}$  which is evaluated more easily than the expression in (33).

#### Evaluating $\beta_{ik}$

Letting  $F_2^{-1}\{\cdot\}$  denote the 2D inverse Fourier transform [15], and using capital letters to denote Fourier transforms, where the vector  $\boldsymbol{\omega} = (\omega_1 \ \omega_2)'$  represents a point in the spatial frequency domain,

$$\begin{aligned} a(\boldsymbol{\epsilon}) &= F_2^{-1}\{A(\boldsymbol{\omega})\} \\ &= \int_{-\infty}^{\infty} \int_{-\infty}^{\infty} A(\omega_1, \omega_2) e^{j2\pi(\omega_1 \epsilon_1 + \omega_2 \epsilon_2)} d\omega_1 d\omega_2. \end{aligned} \quad (34)$$

By taking partial derivatives of both sides,  $\beta_{ik}$  may be obtained in terms of  $A(\boldsymbol{\omega})$ , the 2D Fourier transform of the ambiguity function  $a(\boldsymbol{\epsilon})$

$$\beta_{ik} = -4\pi^2 F_2^{-1}\{\omega_i \omega_k A(\boldsymbol{\omega})\}_{\boldsymbol{\epsilon}=0} \quad i, k \in \{1, 2\}. \quad (35)$$

In a moment, an expression is developed for the Fourier transform of the ambiguity function as a product of several 2D Fourier transforms. First, note that the ambiguity function  $a(\boldsymbol{\epsilon})$  may be written as

$$a(\boldsymbol{\epsilon}) = \mathbf{B}(\mathbf{R}f * h * \mathbf{R}f^{\sim} * h * \xi) \quad (36)$$

where  $*$  denotes 1D convolution in the  $t$  variable in Radon

space,  $f(\mathbf{x}) = d \cdot f_o(\mathbf{x})$  is the object situated at the origin with contrast  $d$ ,  $h(t)$  is the measurement aperture,  $\tilde{f}(x_1, x_2) \triangleq f(-x_1, -x_2)$ , and  $\mathbf{B}$  and  $\mathbf{R}$  are the back-projection and Radon transform operators discussed in Section II. In this expression, the Radon-space function  $\xi(t, \theta)$  is a sampling function that allows the limited-view CBP, with an integral over the interval  $\theta \in [\pi/2 - \Delta, \pi/2 + \Delta)$ , to be written as a CBP over the continuous interval  $0 < \theta \leq \pi$ .

*Claim 1:* In the continuous-view measurement case,  $\xi$  in (36) is given by

$$\xi_{\Delta}(t, \theta) = \delta(t) \cdot \text{rect}\left(\frac{\pi - 2\theta}{4\Delta}\right) \quad 0 < \Delta \leq \frac{\pi}{2} \quad (37)$$

where

$$\text{rect}(\tau) = \begin{cases} 1 & \text{if } |\tau| \leq \frac{1}{2} \\ 0 & \text{otherwise.} \end{cases} \quad (38)$$

The function  $\xi_{\Delta}: Y \rightarrow R$  in (37) is a truncated impulse sheet in Radon space, that is, it is the product of an impulse sheet along the  $\theta$  axis and a 2D function that is zero everywhere except for  $\theta \in [\pi/2 - \Delta, \pi/2 + \Delta)$ , where it equals unity.

*Proof:* See Appendix A.

Since the ambiguity function may be written as the CBP shown in (36), its Fourier transform  $A(\boldsymbol{\omega})$  in (35) may be obtained by using the fact that CBP may be written as a 2D convolution (Davison and Grunbaum [19], Tuy [20]). In particular, letting  $F(\boldsymbol{\omega})$  denote the 2D Fourier transform of  $f(\mathbf{x}) = d \cdot f_o(\mathbf{x})$ , it is shown in Appendix B that

$$A(\boldsymbol{\omega}) = |F(\boldsymbol{\omega})|^2 R_h^2(\boldsymbol{\omega}) B_{\xi}(\boldsymbol{\omega}). \quad (39)$$

Here  $B_{\xi}(\boldsymbol{\omega})$  is the 2D Fourier transform of  $b_{\xi}(\mathbf{x})$ , the back-projection of the Radon-space function  $\xi(t, \theta)$ . In (39),  $R_h(\boldsymbol{\omega})$ , due to the measurement aperture  $h(t)$ , is a circularly symmetric function [since  $h(t)$  is  $\theta$ -independent] with a central section given by  $H(\omega)$ , the 1D Fourier transform of  $h(t)$ . The 2D inverse Fourier transform of  $R_h(\boldsymbol{\omega})$  will be denoted as  $r_h(\boldsymbol{\omega})$ . The relationships in (36) and (39) are illustrated schematically in Fig. 4.

Combining (35) and (39), the second partial derivative of the ambiguity function  $a(\boldsymbol{\epsilon})$  evaluated at the origin, is given by

$$\begin{aligned} \beta_{ik} &= -4\pi^2 F_2^{-1}\{\omega_i \omega_k |F(\boldsymbol{\omega})|^2 R_h^2(\boldsymbol{\omega}) B_{\xi}(\boldsymbol{\omega})\}_{\boldsymbol{\epsilon}=0} \\ & \quad i, k \in \{1, 2\}. \end{aligned} \quad (40)$$

#### The Back-Projection $b_{\xi}(\mathbf{x})$ and Its 2D Fourier Transform

The back-projection of the truncated impulse sheet  $\xi_{\Delta}(t, \theta)$  is derived in Appendix A, and is given by

$$b_{\xi, \Delta}(\mathbf{x}) = \begin{cases} \frac{1}{\|\mathbf{x}\|} & \text{if } |\phi| \leq \Delta \\ 0 & \text{otherwise} \end{cases} \quad (41)$$

where  $\phi$  is the angular polar coordinate of  $\mathbf{x}$ ,  $\phi \in [-\pi/2, \pi/2)$ . The region of the  $\mathbf{x}$  plane where  $b_{\xi, \Delta}(\mathbf{x})$  is positive is indicated in Fig. 5(a). In the special case of full-view measurements, where  $\Delta = \pi/2$  the back-projection of  $\xi_{\pi/2}$  is positive everywhere and is given by the function  $1/\|\mathbf{x}\|$ .

The 2D Fourier transform of  $b_{\xi, \Delta}(\mathbf{x})$  is also derived in Ap-

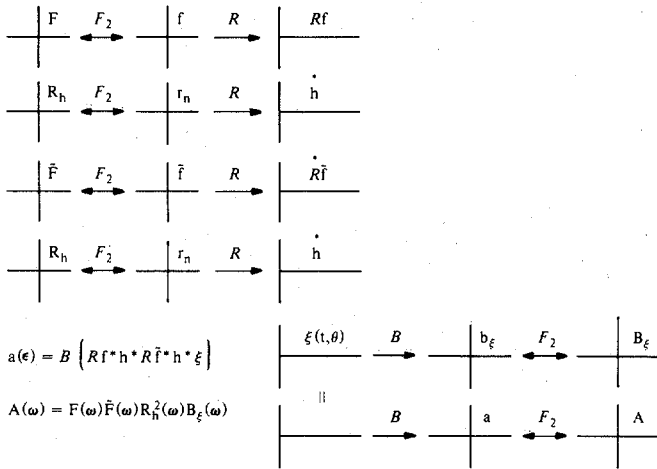


Fig. 4. Schematic representation of the transform relationships.

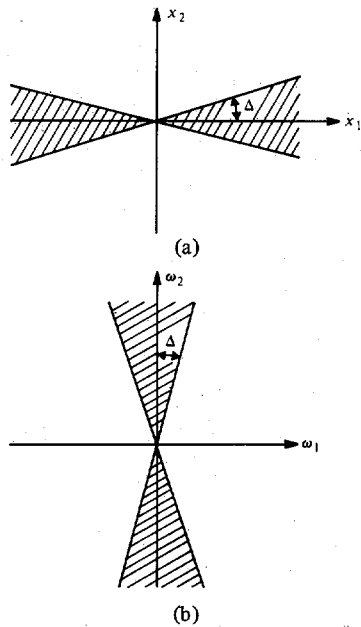


Fig. 5. (a) Region where  $b_{\xi, \Delta}(\mathbf{x})$  is nonzero. (b) Region where  $B_{\xi, \Delta}(\boldsymbol{\omega})$  is nonzero.

pendix A, and is given by

$$B_{\xi, \Delta}(\boldsymbol{\omega}) = \begin{cases} \frac{1}{\|\boldsymbol{\omega}\|} & \text{if } \left| \psi - \frac{\pi}{2} \right| \leq \Delta \\ 0 & \text{otherwise} \end{cases} \quad (42)$$

where  $\psi$  is the angular polar coordinate of  $\boldsymbol{\omega}$ ,  $\psi \in [0, \pi)$ . The subset of the  $\boldsymbol{\omega}$  plane where  $B_{\xi, \Delta}(\boldsymbol{\omega})$  is positive is shown in Fig. 5(b); in the full-view case, it is positive everywhere and equals  $1/\|\boldsymbol{\omega}\|$ .<sup>3</sup>

Summarizing, an expression is given in (25) for the ML location estimate error covariance as a linear combination of conditional error covariances. The probabilities  $p_j$  in this expres-

<sup>3</sup>In the discrete-view measurement case,  $\xi$  in (36) is a train of  $N$  two-dimensional impulses uniformly spaced on the interval  $[0, \pi)$  along the  $\theta$  axis in  $Y$ . The back-projection  $b_{\xi}(\mathbf{x})$  and its Fourier transform  $B_{\xi}(\boldsymbol{\omega})$ , in this case, are both *spoke functions* [6], [14].

sion are computed from (27) or some approximation thereof, and the conditional error covariances are approximated by (29) when  $j \neq 0$ , and bounded as shown in (31) when  $j = 0$ , where the Fisher's information matrix entries in (33) are obtained using the inverse Fourier transform shown in (40). Prior to evaluating these expressions, the regions  $C_j \subset C$  and points  $\boldsymbol{\gamma}_i \in C_j$  must be chosen appropriately. In the next section, the constant-density disk object in Example 1 is reconsidered; systematic use of the performance analysis machinery just developed is demonstrated through this example. In particular, the ambiguity function for the object localization problem is evaluated, the regions  $C_j$  and point  $\boldsymbol{\gamma}_j$  are selected based on an examination of this function, and an approximation to the estimate error covariance  $\Lambda_e$  is evaluated for several different measurement noise levels and different values of object radius. As will be demonstrated, localization performance is characterized by a clear threshold effect; in particular, it is possible to identify, for a given object contrast and a given measurement noise level, the smallest object size that can be located reliably.

In closing, it should be noted that the problem of detecting a constant density object having *known location* by examining a reconstructed image has been considered by Hanson [6], who empirically identified the relationship between minimum detectable contrast and object diameter. It is well known [16] that when the noise in projection measurements is white, the noise in the reconstructed image is nonwhite. Hanson demonstrated the necessity of appropriate 2D filtering of the reconstructed imagery; without such filtering, human interpreters have difficulty in detecting large low contrast objects in the presence of colored reconstruction noise. The "appropriate" 2D filter essentially corresponds to a whitening filter [13], which undoes the noise correlating effect of the CBP operation.

#### IV. EXAMPLE

Reconsider Example 1 in Section II, involving a constant-density object on a disk of radius  $R$  centered at the point  $\mathbf{c}_a \in C \subset R^2$ , and suppose that the set  $C$  of possible object locations is itself a disk of radius  $T$ .

$$C = \{\mathbf{x} : \|\mathbf{x}\| \leq T\}. \quad (43)$$

Since many of the expressions in this section will depend on  $T$  and  $R$  only through their ratio, the parameter  $k$  is defined

$$k \triangleq T/R. \quad (44)$$

When the object is located at the origin, its density function is given by

$$d \cdot f_o(\mathbf{x}) = \begin{cases} d & \text{if } \|\mathbf{x}\| \leq R \\ 0 & \text{otherwise.} \end{cases} \quad (45)$$

This density function is circularly symmetric and consequently its 2D Fourier transform is also circularly symmetric [15]. Letting  $f(r)$  and  $F(\rho)$  denote the density function in (45) and its 2D Fourier transform as functions of their radial polar coordinate only,

$$f(r) = d \cdot \text{rect}(r/2R) \quad (46)$$



where  $\text{rect}(t)$  is defined in (38), and  $F(\rho)$ , known as the Fourier-Bessel or Hankel transform of order zero of  $f(r)$  [15], is given by

$$F(\rho) = 2\pi \int_0^\pi f(r) J_0(2\pi r \rho) r dr = (Rd/\rho) J_1(2\pi R\rho). \quad (47)$$

Here,  $J_0(\cdot)$  and  $J_1(\cdot)$  are Bessel functions of the first kind of order zero and one, respectively.

In this example, the full-view measurement case is considered—the measurements are noisy projections that are band-limited, i.e., smoothed by  $2W$  times the sinc aperture in (5). The 1D Fourier transform of  $h(t)$  is

$$H(\omega) = \text{rect}(\omega/2W). \quad (48)$$

In the full-view case being considered,

$$B_{\xi, \Delta}(\omega) = \frac{1}{\|\omega\|}. \quad (49)$$

The ambiguity function and its 2D Fourier transform in (39) are both circularly symmetric. Denoting them respectively by  $a(r)$  and  $A(\rho)$  as functions of their radial polar coordinates only,  $a(r)$  may be expressed in terms of the inverse Hankel transform [15] as

$$a(r) = 2\pi \int_0^\infty A(\rho) J_0(2\pi r \rho) \rho d\rho. \quad (50)$$

From (39), (47)–(49), and a change of variable,

$$\begin{aligned} a(r) &= 2\pi d^2 R^3 \int_0^{RW} J_1^2(2\pi \rho) J_0(2\pi r \rho / R) (1/\rho^2) d\rho \\ &\triangleq E a^*(r/R, RW) \end{aligned} \quad (51)$$

where  $E$  is the energy in the Radon transform (i.e., the signal part of the measurements),

$$E \triangleq \int_0^\pi \int_{-R}^R \{2d\sqrt{R^2 - t^2}\}^2 dt d\theta = \frac{16}{3} \pi d^2 R^3. \quad (52)$$

The normalized ambiguity function  $a^*$  is seen to depend on the spatial bandwidth  $W$  only through the radius-bandwidth product  $RW$ ;  $a^*$  is plotted in Fig. 6 for several values of  $RW$ . The radius-bandwidth product has a simple interpretation; it equals the object radius  $R$ , expressed as a number of wavelengths at frequency  $W$ . As Fig. 6 indicates, the general shape of the location ambiguity function is virtually independent of the value of radius-bandwidth product for values of  $RW$  in excess of 0.5, i.e., whenever the object diameter exceeds one wavelength at frequency  $W$ . In this example, performance is analyzed for radius-bandwidth products in excess of 0.5.

As was discussed in Section III, an approximation to the error covariance of the location estimate may be obtained by partitioning the parameter space  $C$  into  $M$  nonoverlapping regions  $C_j$ , and then evaluating the linear combination of conditional error covariances in (30), where  $\mathcal{Y}_j$  is a point in  $C_j$ . In this example,  $C$  is a disk of radius  $T$ , and it is partitioned into square regions of side length  $2R$ , centered at the points

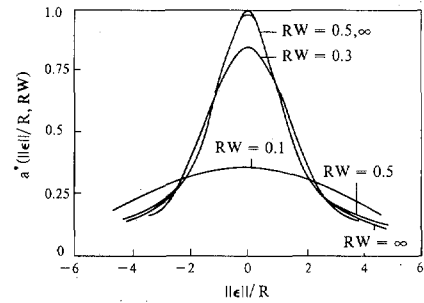


Fig. 6. Central section of the normalized location ambiguity function.

$$\mathcal{Y}_j \in \{(2Rm, 2Rn) : (2Rm, 2Rn) \in C, m, n \text{ integer}\}. \quad (53)$$

This value of region size, although somewhat arbitrarily chosen, appears to be appropriate in view of the discussion in Section III and the form of the ambiguity function in Fig. 6 for  $RW > 0.5$ . In particular, each region  $C_j$  is small enough so that the log likelihood function  $L(\epsilon)$  can, for the purposes of global error analysis, be reasonably approximated by a piecewise constant function on regions  $C_j$ , yet large enough so that the statistical correlation between random variables  $L_i$  and  $L_j$ ,  $i \neq j$ , is small enough to allow an easy approximation to the probabilities  $p_j$  in (27), as is discussed shortly.

When the regions  $C_j$  are squares with side length  $2R$ , the number of regions in the disk  $C$  is approximately the ratio of the disk area  $\pi T^2$  to the region area  $4R^2$ , or using  $k$  in (44),

$$M \approx \frac{\pi T^2}{4R^2} = \frac{\pi}{4} k^2. \quad (54)$$

To proceed with evaluation of the approximate error covariance in (30), the probabilities  $p_j$  in (27) and the conditional error covariance  $\Lambda_0$  are needed. Considering the first of these, the set of random variables  $L_j = L(\mathcal{Y}_j)$ ,  $j = 0, 1, \dots, M-1$  are jointly Gaussian and as indicated by (26) and Fig. 6, have nonzero mean and nonzero covariance. Because the log likelihood function values  $L_j$  are correlated, determination of the probabilities  $p_j$  in (27) is computationally intensive, involving an  $M$ -dimensional numerical integration if evaluated directly. The analysis of this example will exploit the fact that the coefficient of correlation between  $L_i$  and  $L_j$ ,

$$\begin{aligned} \lambda_{ij} &= \frac{E\{(L_i - E\{L_i\})(L_j - E\{L_j\})\}}{[E\{(L_i - E\{L_i\})^2\} E\{(L_j - E\{L_j\})^2\}]^{1/2}} \\ &= \frac{1}{E} a(\mathcal{Y}_i - \mathcal{Y}_j), \end{aligned} \quad (55)$$

is always less than 0.35, for  $i \neq j$ . This correlation is neglected, and the random variables  $L_i$  and  $L_j$  are approximated as being uncorrelated when  $i \neq j$ . This is equivalent to assuming that the ambiguity function equals zero for  $|r/R| \geq 2$ .

The error introduced by this approximation is minor, and, in fact, this approximation makes the results conservative in the following sense. When the  $L_j$  are approximated as being uncorrelated, and conditioned on  $\mathbf{c}_a = \mathcal{Y}_0$ , the probability masses at the points  $\mathcal{Y}_j$  are identical for  $j = 1, 2, \dots, M-1$ . That is, conditioned on the peak lying in an incorrect region, under this approximation it is equally likely to occur in any one of the regions  $C_1, C_2, \dots, C_{M-1}$ , and

$$p_j = \frac{1 - p_0}{M - 1} \quad j = 1, 2, \dots, M - 1. \quad (56)$$

Actually, however, since the ambiguity function is positive and monotonically decreasing away from the point  $\mathbf{c}_a$ , if the peak lies in an incorrect region, it will be more likely to lie close to the location of the true object, rather than far away.

Under the approximation of uncorrelated  $L_j$ , a simple approximation for the probabilities  $p_j$  in (27) may be obtained. If the true object location  $\mathbf{c}_a$  is  $\gamma_0$ , then the union bound [13] may be used to approximate the probability of error  $1 - p_0$  as

$$\begin{aligned} \text{Prob}(\text{error}) &= 1 - p_0 = 1 - \text{Prob} \{L_0 > L_j, \forall j \neq 0\} \\ &\approx \frac{M - 1}{\sqrt{2\pi E/N_o}} \exp\left(-\frac{E}{2N_o}\right). \end{aligned} \quad (57)$$

While the last line is an upper bound on the error probability, it is tight for values of  $E/N_o$  in excess of 5 or so [13]; since the performance is assessed for SNR values greater than 5 in this example, the expression in (57) is treated as an *accurate approximation* to the error probability, rather than as a bound.

Using (56), the approximate error covariance in (30) becomes

$$\Lambda_e \approx \Lambda_0 p_0 + (1 - p_0) \sum_{j=1}^{M-1} \left(\frac{1}{M-1}\right) (\gamma_j - \gamma_0)(\gamma_j - \gamma_0)'. \quad (58)$$

The  $(M - 1)$ -term summation corresponds to the second moment about the point  $\gamma_0$  of a discrete 2D random variable which is equally likely to occur at any one of  $M - 1$  points on the lattice

$$\begin{aligned} \{(2Rm, 2Rn) : (2Rm, 2Rn) \\ \in C, m, n \text{ integer, not both zero}\}. \end{aligned} \quad (59)$$

This moment is well approximated by considering a 2D continuous random variable uniformly distributed on the disk  $C$ ; it has a second moment about the point  $\gamma_0 = \mathbf{c}_a$  of

$$\begin{bmatrix} T^2/4 + c_{a1}^2 & c_{a1} c_{a2} \\ c_{a1} c_{a2} & T^2/4 + c_{a2}^2 \end{bmatrix} \quad (60)$$

where  $\mathbf{c}_a = (c_{a1} \ c_{a2})'$ . For the sake of illustration, only the case where the object is located at the origin is considered here, in which case (58) becomes

$$\Lambda_e \approx \Lambda_0 p_0 + (1 - p_0)(T^2/4)I \quad (61)$$

where  $I$  is the  $2 \times 2$  identity matrix.

The final step in the performance characterization is the local error analysis involving computation of the  $2 \times 2$  Fisher's information matrix  $J$ . From (33), the  $ik$ th entry in the Fisher's information matrix is  $-(2/N_o)\beta_{ik}$ , where from (40), (42), (47), and a change to polar coordinates  $(\rho, \psi)$ ,

$$\beta_{ik} = -(2\pi R d)^2 \int_0^\pi \nu(\psi) d\psi \int_{-\infty}^\infty J_1^2(2\pi R|\rho|) H^2(\rho) d\rho \quad (62)$$

where

$$\nu(\psi) = \begin{cases} \cos^2 \psi & \text{if } i = k = 1 \\ \sin^2 \psi & \text{if } i = k = 2 \\ \cos \psi \sin \psi & \text{if } i \neq k. \end{cases} \quad (63)$$

Performing the integration with respect to  $\psi$ ,  $\beta_{12} = \beta_{21} = 0$ , and

$$\begin{aligned} \beta_{ii} &= -2R(\pi d)^2 \int_0^{2\pi RW} J_1^2(\rho) d\rho \triangleq -(3\pi/8R^2) E\mu(RW) \\ i &\in \{1, 2\} \end{aligned} \quad (64)$$

where  $E$  is the Radon transform energy given in (52). By the symmetry of the problem, then, the Fisher's information matrix is a scalar times the  $2 \times 2$  identity matrix, and from (31) the diagonal entries of the conditional error covariance  $\Lambda_0$  are bounded by

$$[\Lambda_0]_{ii} \geq -\frac{N_o}{2\beta_{ii}} \quad i \in \{1, 2\}. \quad (65)$$

A plot of the function  $\mu(RW)$  in (64) for  $RW \in [0, 10]$  is shown in Fig. 7. Note that  $\mu(RW)$  is a monotonically nondecreasing function and as  $RW$  approaches infinity (i.e., for a fixed object size  $R$ , as the measurement system bandwidth  $W$  approaches infinity),  $\mu(RW)$  becomes infinite. This implies that the ambiguity function  $a(\mathbf{r})$  is not twice differentiable in the limit  $RW \rightarrow \infty$  [ $s(t, \theta)$  approaches a half-ellipse which has points of infinite first derivative], and the Cramer-Rao lower bound in (65) degenerates to zero. This is a well-known phenomenon that also arises in radar performance analysis in the limiting case of infinite measurement system bandwidth [21]. In any practical case, smoothing or bandlimiting of the projection measurements always occurs, so that the aperture  $h(t)$  is nonimpulsive and the radius-bandwidth product is finite.

Denoting by  $\sigma_e^2$  the diagonal entries in the approximation to  $\Lambda_e$  in (30), it follows from (61) and (65) that

$$\begin{aligned} \sigma_e^2 &\geq -\frac{N_o}{2\beta_{ii}} p_0 + (1 - p_0) \frac{T^2}{4} \\ &= -\frac{N_o}{2\beta_{ii}} + \left[\frac{T^2}{4} + \frac{N_o}{2\beta_{ii}}\right] (1 - p_0). \end{aligned} \quad (66)$$

Finally, by incorporating the approximation for  $(1 - p_0)$  in (57), approximating  $M - 1$  as shown in (54), and using (64), the error covariance  $\sigma_e^2$  normalized by  $T^2$ , is approximately lower bounded by the following quantity.

$$\begin{aligned} \left(\frac{\sigma_{LB}}{T}\right)^2 &= \frac{4}{3\pi k^2 (E/N_o) \mu(RW)} \\ &+ \left[\frac{1}{4} - \frac{4}{3\pi k^2 (E/N_o) \mu(RW)}\right] \frac{\pi k^2}{4\sqrt{2\pi E/N_o}} \\ &\cdot \exp\left(-\frac{E}{2N_o}\right). \end{aligned} \quad (67)$$

The dependence of the localization performance on the object size  $R$ , for a fixed value of density, may be illustrated by substituting  $E$  from (52) and considering (67) for fixed values of  $d^2/N_o$ . The inverse of this normalized error variance is plotted in Fig. 8 versus normalized object size  $R/T$  for three

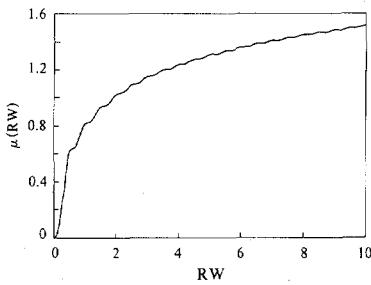
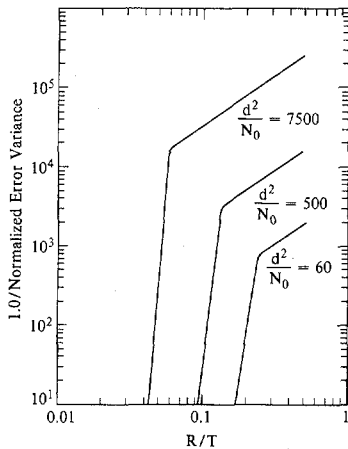
Fig. 7.  $\mu(RW)$  versus radius-bandwidth product.

Fig. 8. Localization performance versus normalized object size.

values of  $d^2/N_o = 60, 500, \text{ and } 7500$ , with  $W = 50$ . These curves depict a very strong threshold behavior in localization performance; for a given object contrast  $d$  and noise level  $N_o$ , there exists a clearly defined smallest sized object that can be located reliably from noisy projection data.

Summarizing, the analysis of this section has focused on the problem of using noisy, full-view projection measurements of a cross-section to estimate the location of a constant-density disk object. A framework has been presented for evaluating the estimation performance. Quantitative performance analyses may also be carried out within this framework for the cases of limited-view ( $\Delta < \pi/2$ ) and discrete-view projection measurements, as well as for other object models, such as the Gaussian object mentioned in Section II [14].

## V. COMPUTER SIMULATION

A limited amount of noisy projection data were generated by computer and were processed using a CBP algorithm for two purposes: 1) to determine the 2D log likelihood function for the unknown object location, and 2) by using a conventional reconstruction kernel, to develop an estimate for the 2D cross-sectional density function.

The specific example considered in these simulations is the simple disk object of Example 1, having radius  $R$  and situated within the disk  $C$  of radius  $T$ . The object size is chosen so that  $k = T/R$  in (44) equals 5. For notational convenience, the geometry is normalized so that  $T$  equals unity, in which case the object has a radius  $R = 0.2$ . The actual object is located at the point  $(0.2, 0.4)$ ; an image representation of this cross section is shown in Fig. 9.

A total of 105 projection measurements were calculated,

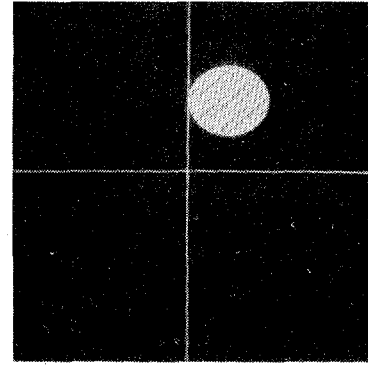


Fig. 9. Image representation of the single-object cross-sectional density function.

corresponding to infinitely narrow line integral measurements ( $RW = \infty$ ) using a parallel-ray measurement geometry. Five views were generated at angles  $\theta_j = j\pi/5, j = 0, 1, \dots, 4$ . Within each view, integrals were calculated along 21 parallel lines with  $t$  values satisfying  $t_m = 0.1m, m = -10, -9, \dots, 10$ , corresponding to an inter-ray spacing of 0.1.

Pseudorandom white noise samples having zero mean and adjustable variance  $\sigma^2$  were added to the 105 line integrals to provide noisy measurements  $y(t_m, \theta_j)$ . The measurement signal-to-noise ratio (SNR) in dB is defined as

$$\text{SNR} \triangleq 10 \log_{10} (E_d / 105 \sigma^2) \quad (68)$$

where  $E_d$  is the Radon transform energy

$$E_d = \sum_{j=0}^4 \sum_{m=-10}^{10} g^2(t_m, \theta_j) \quad (69)$$

and  $g(t, \theta)$  is the Radon transform of the simulated density function.

The noisy data  $y(t_m, \theta_j)$  were processed to develop  $240 \times 240$  pixel images (16 grey levels per pixel) by using the CBP equation

$$a(\mathbf{x}) = \sum_{j=0}^4 \sum_{m=-10}^{10} y(t_m, \theta_j) z(t_m - \mathbf{x}'\theta_j, \theta_j) \quad (70)$$

$$|x_1|, |x_2| \leq 1.$$

The convolving kernel  $z(t, \theta)$  is given by one of two functions, depending on whether the log likelihood function or a reconstructed image is being computed. In each case, a piecewise linear approximation to the ideal continuous convolving kernel was used in order to reduce the computation time.

Since the disk object is circularly symmetric, the convolving kernel for the log likelihood function evaluation, denoted by  $z_{LL}(t)$ , is  $\theta$ -independent, and is given by the following piecewise linear approximation to the projection of a disk with a radius of 0.2.

$$z_{LL}(t) = \begin{cases} 2\sqrt{(0.2)^2 - t^2} & \text{if } |t| \leq 0.2, t \text{ an integer multiple of } 0.02 \\ 0 & \text{if } |t| > 0.2, t \text{ an integer multiple of } 0.02 \end{cases} \quad (71)$$

If  $t$  is not an integer multiple of 0.02, the value of  $z_{LL}(t)$  is obtained by linear interpolation of its two nearest values in (71).

In calculating a reconstructed image, the convolving kernel, denoted  $z_I(t)$ , is the  $\theta$ -independent kernel presented in Shepp and Logan [1], and is given by the piecewise linear function

$$z_I(t) = \frac{1}{10\pi} \frac{1}{0.25 - 100t^2} \quad \text{if } t \text{ is an integer multiple of } 0.1. \quad (72)$$

If  $t$  is not an integer multiple of 0.1, the value of  $z_I(t)$  is obtained by linear interpolation of its two nearest values in (72).

In this simulation, two measurement SNR noise levels (68) were used, namely 0 and -3 dB, and the same noise samples at each level were used with both convolving kernels. To simplify interpretation of the images, the image values are first normalized to the interval [0, 1] with 0 and 1 corresponding to black and white, respectively, and the 16-level gray scale is then uniformly distributed on the interval [0.6, 1] or [0.75, 1] as indicated, resulting in the blackening out of lower intensity regions.

Fig. 10(a) and (b) corresponds to the log likelihood function [kernel in (71)] and reconstructed image [kernel in (72)] respectively, when the measurement SNR is 0 dB and the gray scale is distributed on the interval [0.6, 1]. Fig. 10(c) and (d) is the likelihood function and reconstructed image for an SNR equal to -3 dB, with the gray scale distributed on the interval [0.75, 1]. Notice that for both measurement noise levels the image reconstruction kernel  $z_I(t)$ , because of its higher gain at high frequencies, leads to spurious peaks in the reconstruction, all having approximately the same size and distributed throughout the cross section. The log likelihood function, on the other hand, has only one peak in the 0 dB case, occurring at (0.24, 0.34), which is very close to the true object location (0.2, 0.4). In the -3 dB case, the log likelihood function has several secondary peaks, but the major peak, located at (0.18, 0.49), is also close to the true location.

As indicated by Fig. 10(b) and (d), object detection and localization is difficult by direct visual examination of noisy reconstructed imagery. As discussed at the end of Section III, image post-processing to extract object related information has been considered by Hanson [6] and others. In the presence of projection measurement noise that is white, the reconstructed image noise is nonwhite [16], in which case optimal object localization from reconstructed imagery involves 2D noise prewhitening followed by matched filtering. A sub-optimal approach to post-processing a reconstructed image for object identification purposes, and one that is quite often used in image processing, is to perform matched filtering assuming that the measurement noise is white. For the present problem, this corresponds to performing 2D matched filtering on the reconstructed image using a disk object template.

The reconstructed images in Fig. 10(b) and (d) were post-processed by treating the reconstructed image noise as white, and performing matched filtering to locate a constant-density object of radius 0.2. The following 2D matched filter template was used.

$$f_c(\mathbf{x}) = \begin{cases} 1 & \text{if } |\mathbf{x}| \leq 0.2 \\ 0 & \text{otherwise.} \end{cases} \quad (73)$$

The image in Fig. 11(a) is the result of matched filtering the image in Fig. 10(b) with  $f_c(\mathbf{x})$ , with the gray scale distributed on [0.6, 1]. Similarly, Fig. 11(b) is the result of matched filtering the image in Fig. 10(d), with the gray scale distributed on [0.75, 1]. These two images are seen to be very similar to the log likelihood images in Fig. 10(a) and (c), although the log likelihood images were computed directly in much less time than the two-step process of first reconstructing and then performing 2D matched filtering. The similarity of these images is due in part to the robustness of the matched filter—even though the matched filter in (73) is optimal only in the presence of white image noise, its performance is very robust to the presence of nonwhite noise.

## VI. CONCLUSIONS

In this paper the problem has been investigated of using ML estimation methods in order to locate a single object whose geometry is known precisely *a priori*. An approximate expression was developed in Section III for the location estimate error covariance, reflecting contributions due to both local and global errors. In Section IV, an approximation to this expression was evaluated for a constant-density disk object; the results of this example indicate that for a given value of object contrast  $d$  and noise spectral level  $N_o$ , there exists a minimum value of object size for which reliable localization may be performed.

A computer simulation was also presented which illustrates the evaluation of the log likelihood function for the localization of a constant-density disk object from computer-generated noisy projections, as well as the evaluation of a reconstructed image from the same noisy measurements. These simulations demonstrate that at high noise levels and with a limited number of projections, an object in a cross section is much more easily discerned by examining the log likelihood function than by examining a reconstructed image that has not undergone time-consuming post-processing.

The focus of Part I was the simple problem of locating a single object of known contrast and density distribution  $f_o(\mathbf{x})$ , superimposed on a *known* background field that contains no additional objects. By casting the problem in this framework, insight was obtained about the CBP computational structure of the log likelihood function evaluation, and the performance of the ML estimator was characterized. In Part II, robustness issues are addressed, in particular, the robustness of these procedures when applied to less idealized versions of the problem that take into account, for example, that the object size, shape, or detailed density variations may differ from those that are assumed, or that additional unmodeled objects may be present within the cross section.

## PART II

### ROBUSTNESS ANALYSIS

#### I. INTRODUCTION

In Part I, the problem of locating an object in a cross section using projection measurements was considered; the perfor-

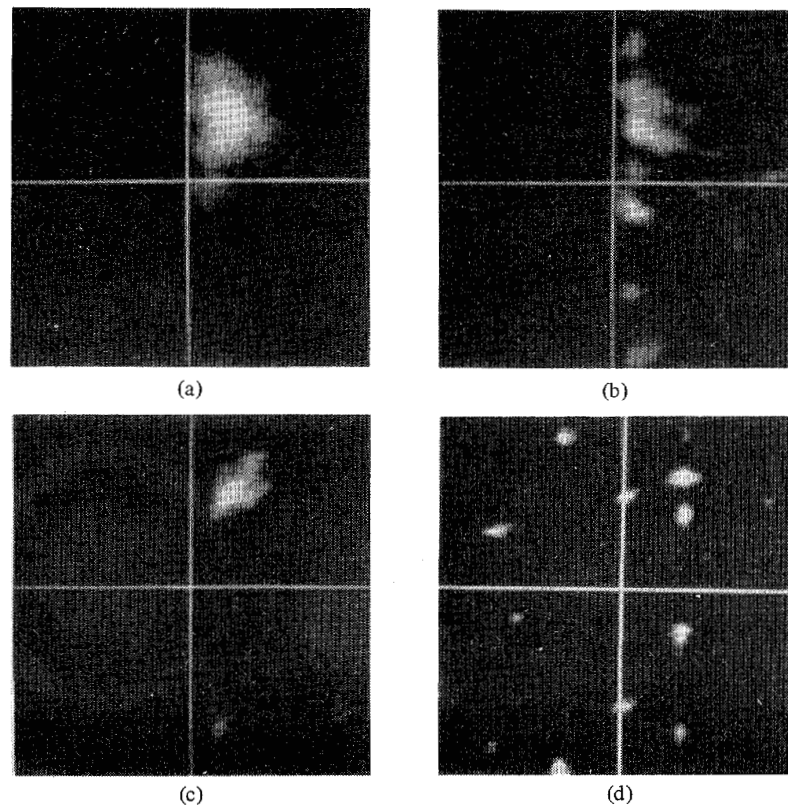


Fig. 10. (a) Log likelihood function, SNR = 0 dB, scale = [0.6, 1.0]. (b) Reconstructed image, SNR = 0 dB, scale = [0.6, 1.0]. (c) Log likelihood function, SNR = -3 dB, scale = [0.75, 1.0]. (d) Reconstructed image, SNR = -3 dB, scale = [0.75, 1.0].

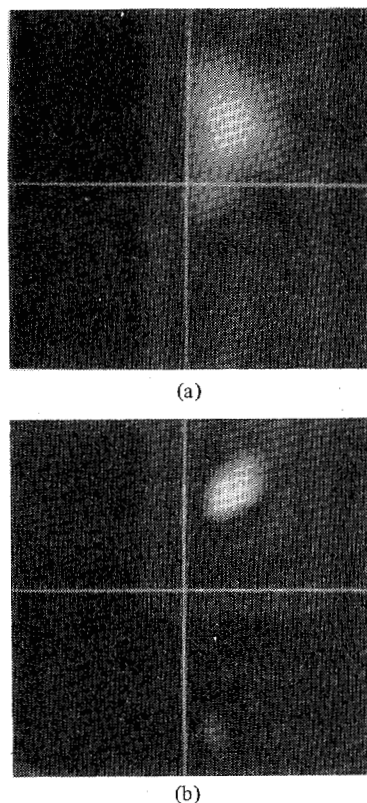


Fig. 11. (a) Result of convolving the image in Fig. 10(b) with  $f_c(\mathbf{x})$ ; scale = [0.6, 1.0]. (b) Result of convolving the image in Fig. 10(d) with  $f_c(\mathbf{x})$ ; scale = [0.75, 1.0].

mance was analyzed and illustrated with an example and simulations. A number of assumptions were made in the course of this development, including the following.

- The measurements are projections observed through a 1D measurement aperture and corrupted by additive white noise; evaluation of the projection at any point is given by the integral of the density field along a straight line, see (I.1) and (I.4).
- The cross-sectional field consists of exactly one object profile superimposed on a background field that is known exactly, see (I.3).
- The boundary shape and detailed density variations corresponding to the object are known precisely, i.e., the contrast parameter  $d$  and the object  $f_o(\mathbf{x})$  are assumed to be known, see (I.3).

(1)

These assumptions were made in Part I so that insight into the structure and performance of the ML estimator could be more easily obtained. In practice, these assumptions are never completely satisfied, and as a consequence, the localization performance is to some degree adversely affected.

In this part of the paper, several specific types of modeling errors or deviations from the assumptions in (1) are considered, including errors in the modeled object contrast, size, and shape, and in the number of objects that are assumed to be present. For purposes of illustration, Example 1 in Part I is reconsidered, in which the cross section is modeled as the

superposition of a background field  $f_b(\mathbf{x})$  and the single circularly symmetric *disk* object

$$d \cdot f_o(\mathbf{x} - \mathbf{c}; R) = \begin{cases} d & \|\mathbf{x} - \mathbf{c}\| \leq R \\ 0 & \text{otherwise} \end{cases} \quad (2)$$

whose Radon transform  $d \cdot g_o(t - \mathbf{c}'\boldsymbol{\theta}, \theta; R)$  is given in (I.15). The Radon transform subscript "o" refers to the modeled object situated at the origin. In this analysis, modeling errors will be considered by taking the actual cross section to be the superposition of a background field and  $N$  objects, and is represented as

$$f(\mathbf{x}) = f_b(\mathbf{x}) + \sum_{k=1}^N d_k \cdot f(\mathbf{x} - \mathbf{c}_k; \boldsymbol{\zeta}_k). \quad (3)$$

Here, the  $k$ th object has contrast  $d_k$ , location  $\mathbf{c}_k$ , and is characterized (e.g., size, shape, orientation, or detailed density variations) by the finite-dimensional parameter vector  $\boldsymbol{\zeta}_k$ .

Within this framework, the sensitivity of the ML localization performance to various modeling errors is investigated. In particular, object density, size, and shape modeling errors, as well as the presence of one or more unmodeled objects are examined via the following choices for the actual field in (3).

- Density and size modeling error—the actual field is a single ( $N = 1$ ) *disk* object of incorrectly modeled contrast  $d_1$  and radius  $R_1$ .
- Shape modeling error—the actual field is a single ( $N = 1$ ) constant-density object having an *ellipsoidal* boundary with eccentricity  $\lambda$ .
- Presence of unmodeled objects—the actual field is the sum of one correctly modeled disk object (i.e.,  $d_1 = d$  and  $R_1 = R$ ) plus  $N - 1$  disk objects all having the same unknown density  $d_k = d_u$  and radius  $R_k = R_u$ ,  $k = 2, \dots, N$ .

As was the case in Part I, the background field  $f_b(\mathbf{x})$  is assumed in this analysis to be known, and without loss of generality is taken to equal zero. In this case, from (I.1), the Radon transform of the actual field in (3) is

$$g(t, \theta) \triangleq \sum_{k=1}^N d_k \cdot g(t - \mathbf{c}'_k \boldsymbol{\theta}, \theta; \boldsymbol{\zeta}_k). \quad (4)$$

The focus of this analysis will be on global rather than local estimation errors; consequently, the measurement at the point  $(t, \theta)$  in Radon space is taken to be the projection at angle  $\theta$  evaluated at the point  $t$  (i.e., the special case of the measurement model in (I.4) where the measurement aperture  $h(t)$  is impulsive),

$$\begin{aligned} y(t, \theta) &= g(t, \theta) + w(t, \theta) \\ &= \sum_{k=1}^N d_k \cdot g(t - \mathbf{c}'_k \boldsymbol{\theta}, \theta; \boldsymbol{\zeta}_k) + w(t, \theta) \\ &\quad (t, \theta) \in S \subset Y. \end{aligned} \quad (5)$$

For purposes of illustration, only the case of full-view measurements,  $S = Y$ , is considered here.

As shown in Part I, the ML estimate of the object location  $\mathbf{c} \in R^2$  is obtained from noisy projection measurements by locating the maximum of the log likelihood function

$$\begin{aligned} L(\mathbf{c}) &= \frac{2d}{N_o} \int_0^\pi \int_{-\infty}^\infty y(t, \theta) g_o(t - \mathbf{c}'\boldsymbol{\theta}, \theta; R) dt d\theta \\ &\quad - \frac{d^2}{N_o} \int_0^\pi \int_{-\infty}^\infty g_o^2(t - \mathbf{c}'\boldsymbol{\theta}, \theta; R) dt d\theta \end{aligned} \quad (6)$$

where  $d \cdot g_o(t, \theta; R)$  is the modeled object Radon transform. The second term in (6) is a correction for the energy in the Radon-space matched filtering template  $d \cdot g_o(t, \theta; R)$ . Since this energy is  $\mathbf{c}$ -independent and the modeled object radius  $R$  is fixed, the second term in (6) is constant and may be disregarded, as can the scaling factor  $2/N_o$ , leaving

$$L(\mathbf{c}) = d \int_0^\pi \int_{-\infty}^\infty y(t, \theta) g_o(t - \mathbf{c}'\boldsymbol{\theta}, \theta; R) dt d\theta. \quad (7)$$

Using (5), the log likelihood function becomes

$$\begin{aligned} L(\mathbf{c}) &= \sum_{k=1}^N d d_k \int_0^\pi \int_{-\infty}^\infty g(t - \mathbf{c}'_k \boldsymbol{\theta}, \theta; \boldsymbol{\zeta}_k) \\ &\quad \cdot g_o(t - \mathbf{c}'\boldsymbol{\theta}, \theta; R) dt d\theta \\ &\quad + d \cdot \int_0^\pi \int_{-\infty}^\infty w(t, \theta) \cdot g_o(t - \mathbf{c}'\boldsymbol{\theta}, \theta; R) dt d\theta \\ &\triangleq \sum_{k=1}^N d d_k a(\mathbf{c}; \mathbf{c}_k, R, \boldsymbol{\zeta}_k) + n(\mathbf{c}, d, R). \end{aligned} \quad (8)$$

The log likelihood function in (8) is a generalization of the expression in (I.21). The last term is a zero-mean random field with a second moment that depends only on the modeled field, and each of the remaining  $N$  terms corresponds to one of the  $N$  actual objects.

The performance of the location estimator may be characterized by examining the estimate error covariance—such analysis led in Part I to the consideration of two types of errors, namely local and global errors. Local error was characterized using the Cramer-Rao bound in (I.31)-(I.33). Global error was characterized by evaluating an approximation to  $p_j$  in (I.27), the probability that the log likelihood function is a maximum at the  $j$ th of  $M$  points in the plane

$$\{\boldsymbol{\gamma}_j\} \in \{(2Rm, 2Rn) : (2Rm, 2Rn) \in C, m, n \text{ integer}\}. \quad (9)$$

The principle focus of this paper is on characterizing *major* degradation (associated with global types of errors) in the performance due to modeling errors by evaluating a bound on the probability  $p_0$  (one minus the probability of a global error) that applies when the actual and modeled fields differ. Global error analysis in the presence of modeling errors is conceptually identical to the analysis carried out in Part I. In the presence of modeling errors, however, the conditional expected value of the log likelihood function is no longer approximately zero at the points  $\boldsymbol{\gamma}_j, j \neq 0$ . This has the effect of decreasing  $p_0 = \text{prob}\{E_0\}$ , the probability that the log likelihood function peak occurs in the vicinity of the actual object

location. By assessing the manner in which this probability decreases in the presence of particular types of modeling errors, insight into the robustness of the localization procedure may be obtained—this is the approach pursued in this part of the paper.

In the presence of modeling errors,  $\mathbf{m}$ , the conditional expected value of the vector of log likelihood function values on the set of points  $\{\boldsymbol{\gamma}_j\}$ , cannot be approximated as having only a single nonzero element. In this case, a different bound on  $p_j$  than that in (1.57) may be obtained (see Appendix C for the details), and is given by

$$p_j \geq 1 - \sum_{i \neq j} \int_{\Delta_{ij}/\sqrt{2}}^{\infty} \frac{1}{\sqrt{2\pi}} \exp\left(-\frac{x^2}{2}\right) dx$$

$$\triangleq 1 - \sum_{i \neq j} \operatorname{erfc} * \left(\frac{\Delta_{ij}}{\sqrt{2}}\right) \quad (10)$$

where

$$\Delta_{ij} \triangleq \frac{1}{\sigma} (m_j - m_i) \quad (11)$$

$$\operatorname{erfc} * (X) = \int_X^{\infty} \frac{1}{\sqrt{2\pi}} \exp\left(-\frac{x^2}{2}\right) dx \quad (12)$$

and  $\sigma^2$  is the log likelihood function variance at each point  $\boldsymbol{\gamma}_j$ .

In the remainder of Part II, the three specific types of modeling errors listed previously are considered, and for each case the bound on  $p_0$  (one minus the probability of a global error) in (10) is evaluated. In Section II, degradation in the global localization performance is investigated for the case where a single disk object is present but its contrast and size are not known precisely *a priori*. In Section III, the robustness of object localization to shape modeling errors is considered for the case where the actual object is not a disk object, but is instead elongated. In addition to global error robustness analysis, local error robustness is characterized using Cramer-Rao bound analysis. Finally, in Section IV, the sensitivity of the global performance to the presence of one or more unmodeled objects is investigated.

## II. CONTRAST AND SIZE MODELING ERRORS

In this section, the way in which localization performance degrades when the size and contrast of the actual object are known imprecisely is examined. The modeled field is the disk object shown in (2); suppose that the actual field consists of a single *disk* object with radius  $R_a$  and contrast  $d_a$  (not necessarily equal to  $R$  and  $d$ ), and located at the point  $\mathbf{c}_a$ . In this case, the log likelihood function in (8) becomes

$$L(\mathbf{c}, \mathbf{c}_a) = d \cdot d_a \int_0^{\pi} \int_{-\infty}^{\infty} g(t - \mathbf{c}'_a \boldsymbol{\theta}, \theta; R_a)$$

$$\cdot g_o(t - \mathbf{c}' \boldsymbol{\theta}, \theta; R) dt d\theta + n(\mathbf{c}, d, R)$$

$$= d d_a R R_a \int_0^{\pi} \int_{-\infty}^{\infty} g\left(\frac{1}{R_a} (t - \mathbf{c}'_a \boldsymbol{\theta}), \theta; 1\right)$$

$$\cdot g_o\left(\frac{1}{R} (t - \mathbf{c}' \boldsymbol{\theta}), \theta; 1\right) dt d\theta + n(\mathbf{c}, d, R). \quad (13)$$

Letting  $E_0$  represent the Radon-space energy in a unit-contrast, unit-radius disk object [see (1.52)],  $E_a$ , the Radon-space energy in the actual object, is given by

$$E_a = d_a^2 R_a^3 E_0 \quad (14)$$

and (13) may be written as

$$L(\mathbf{c}, \mathbf{c}_a) \triangleq E_a \left(\frac{d}{d_a}\right) a^*\left(\frac{1}{R} (\mathbf{c} - \mathbf{c}_a), R/R_a\right) + n(\mathbf{c}, d, R) \quad (15)$$

where

$$a^*\left(\frac{1}{R} \boldsymbol{\epsilon}, R/R_a\right) = \frac{1}{E_0} \left(\frac{R}{R_a}\right)^2 \int_0^{\pi} \int_{-\infty}^{\infty} g\left(\frac{R}{R_a} t, \theta; 1\right)$$

$$\cdot g_o\left(t - \frac{1}{R} \boldsymbol{\epsilon}' \boldsymbol{\theta}, \theta; 1\right) dt d\theta. \quad (16)$$

Since both the actual and modeled objects are circularly symmetric, the normalized ambiguity function in (16) is also circularly symmetric, and a central section of it is illustrated in Fig. 12 for several values of  $R/R_a$ . Notice that the width of the peak (full width at half maximum), relative to  $R$ , is essentially constant when the modeled size exceeds the actual size, and the width of the peak increases when the actual size exceeds the modeled size. That is, the width is determined essentially by the size of the larger of the modeled and actual objects.

In order to determine how  $p_0$  (one minus the probability of a global error) is affected by incorrect knowledge of the object size, the vector of log likelihood function means  $\mathbf{m}$  on the set of points  $\{\boldsymbol{\gamma}_j\}$  in (9) is evaluated, as is the variance  $\sigma^2$ , conditioned on the actual object location being  $\boldsymbol{\gamma}_0 = \mathbf{0}$  and  $k = T/R$  in (1.44) equal to 10. The mean value of the log likelihood function at the point  $\boldsymbol{\gamma}_j$ , from (15) is

$$m_j = E\{L_j\} = E_a \left(\frac{d}{d_a}\right) a^*\left(\frac{1}{R} \boldsymbol{\gamma}_j, R/R_a\right). \quad (17)$$

The variance of the log likelihood function is

$$\sigma^2 = E\{n^2(\mathbf{c}, d, R)\} = \frac{N_o}{2} E a^*(\mathbf{0}, 1) = E N_o / 2 \quad (18)$$

where  $E$  denotes the energy in the modeled object,  $E = d^2 R^3 E_0$ . Finally, the probability  $p_0$  is bounded as in (10), where

$$\frac{m_j}{\sigma} = \left(\frac{2}{E N_o}\right)^{1/2} E_a \left(\frac{d}{d_a}\right) a^*\left(\frac{1}{R} \boldsymbol{\gamma}_j, R/R_a\right)$$

$$= \left(\frac{2 E_a}{N_o}\right)^{1/2} \left(\frac{R}{R_a}\right)^{-3/2} a^*\left(\frac{1}{R} \boldsymbol{\gamma}_j, R/R_a\right). \quad (19)$$

Notice that, as expected,  $m_j/\sigma$  does not depend on the value of the modeled contrast parameter  $d$ , and depends on the actual contrast  $d_a$  only through the energy term in (14).

Fig. 13 illustrates the lower bound on  $p_0$  versus the measurement SNR ( $10 \log E_a/N_o$ ) for several values of  $R/R_a$ . The best global performance is seen to correspond to perfect object size information ( $R/R_a = 1$ ). In the presence of moderately sized modeling errors, however, the global performance appears to be very robust—even when the modeled object area is in error by 50 percent, the measurement SNR must only be increased by 2 dB or so to maintain a constant global performance.

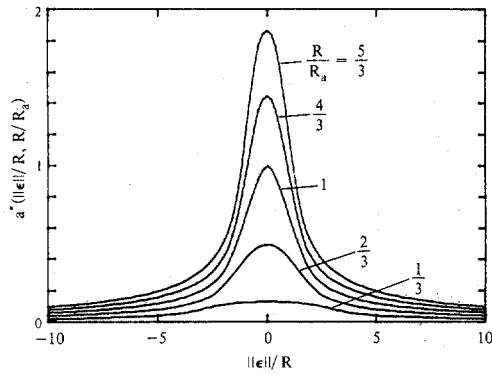


Fig. 12. Normalized location ambiguity function in the presence of size modeling error.

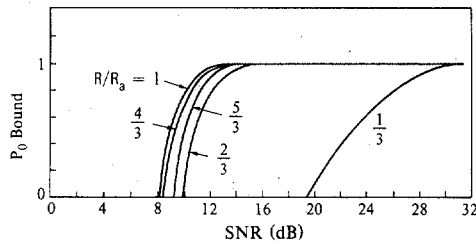


Fig. 13. Lower bound on  $p_0$  versus measurement SNR in the presence of size modeling error.

### III. SHAPE MODELING ERRORS

In this section, the way in which localization performance is adversely affected when the shape of the actual object is not known precisely is evaluated. As before, the modeled object is the disk object in (2); the actual field consists of a single constant density object on an ellipse,

$$d_a \cdot f_o(\mathbf{x}) = \begin{cases} d_a & \text{if } x_1^2/\lambda + \lambda x_2^2 \leq R_a \\ 0 & \text{otherwise} \end{cases} \quad (20)$$

whose Radon transform is denoted by  $g(t, \theta; R_a, \lambda)$ . This object can be thought of as arising by applying the coordinate transformation

$$\tilde{\mathbf{x}} = \begin{bmatrix} \sqrt{\lambda} & 0 \\ 0 & 1/\sqrt{\lambda} \end{bmatrix} \mathbf{x} \quad (21)$$

to a disk object of radius  $R_a$  situated at the origin. Letting  $E_o(\lambda)$  denote the Radon-space energy for the object in (20) when  $d_a = 1$  and  $R_a = 1$ , the Radon-space energy for the actual object is given by

$$E_a = d_a^2 R_a^3 E_o(\lambda). \quad (22)$$

From (8), the log likelihood function for the location estimate is given by

$$\begin{aligned} L(\mathbf{c}, \mathbf{c}_a) &= d d_a \int_0^\pi \int_{-\infty}^{\infty} g(t - \mathbf{c}'_a \boldsymbol{\theta}, \theta; R_a, \lambda) \\ &\quad \cdot g_o(t - \mathbf{c}' \boldsymbol{\theta}, \theta; R) dt d\theta + n(\mathbf{c}, d, R) \\ &\triangleq E_a \left( \frac{d}{d_a} \right) a^* \left( \frac{1}{R} (\mathbf{c} - \mathbf{c}_a), R/R_a, \lambda \right) + n(\mathbf{c}, d, R) \end{aligned} \quad (23)$$

where

$$\begin{aligned} a^* \left( \frac{1}{R} \boldsymbol{\epsilon}, R/R_a, \lambda \right) &= \frac{1}{E_o(\lambda)} \left( \frac{R}{R_a} \right)^2 \\ &\quad \cdot \int_0^\pi \int_{-\infty}^{\infty} g \left( \frac{R}{R_a} t, \theta; 1, \lambda \right) \\ &\quad \cdot g_o \left( t - \frac{1}{R} \boldsymbol{\epsilon}' \boldsymbol{\theta}, \theta; 1 \right) dt d\theta. \end{aligned} \quad (24)$$

As in the previous section, the vector of log likelihood function means  $\mathbf{m}$  and the variance  $\sigma^2$  are evaluated and used in (10) to obtain a bound on the probability  $p_0$  in the presence of shape modeling errors. The mean value of the log likelihood function at the point  $\boldsymbol{\gamma}_j$ , from (23), is

$$m_j = E \{L_j\} = E_a \left( \frac{d}{d_a} \right) a^* \left( \frac{1}{R} \boldsymbol{\gamma}_j, R/R_a, \lambda \right). \quad (25)$$

The variance  $\sigma^2$  is  $EN_o/2$  as previously, where  $E$  denotes the energy in the modeled object  $E = d^2 R^3 E_o$ . The probability  $p_0$  is bounded as in (10), where

$$\begin{aligned} \frac{m_j}{\sigma} &= \left( \frac{2}{N_o E} \right)^{1/2} E_a \left( \frac{d}{d_a} \right) a^* \left( \frac{1}{R} \boldsymbol{\gamma}_j, R/R_a, \lambda \right) \\ &= \left( \frac{2E_a}{N_o} \right)^{1/2} \left( \frac{E_o(\lambda)}{E_o} \right)^{1/2} \left( \frac{R}{R_a} \right)^{-3/2} a^* \left( \frac{1}{R} \boldsymbol{\gamma}_j, R/R_a, \lambda \right). \end{aligned} \quad (26)$$

Fig. 14 illustrates the lower bound on  $p_0$  versus the measurement SNR in dB for actual object eccentricities of 1, 2, 4, and 9. The global localization performance is seen to be quite robust to eccentricity modeling errors.

This robustness to shape modeling errors suggests that in the presence of noncircularly symmetric objects, it may be feasible to employ *recursive* parameter estimation procedures, in which an object's location is first estimated using a relatively simple circularly symmetric object model. Once the location is estimated using a circularly symmetric model, more complicated noncircularly symmetric object models may be used to estimate finer details of the object profile, see [14] for further details.

In this section, a lower bound has been presented for the probability that a *global* error does not occur in estimating the location of an object in the presence of shape modeling errors. As shown in Fig. 14, for a sufficiently high SNR, the location estimate has a high probability of being "close" to the actual object location—more detailed characterization of the estimation error (e.g., addressing the question of whether or not the estimate lies within the actual object boundary) may be obtained by performing Cramer-Rao bound analysis in the presence of model mismatch. In the following section, such an analysis is performed and the *local* error covariance in the presence of shape modeling errors is bounded.

#### Local Error Analysis

As discussed in Part I, the Cramer-Rao bound provides an accurate estimate of the local error covariance matrix  $\boldsymbol{\Lambda}_0$ ; in particular, from (I.31)–(I.33)

$$[\boldsymbol{\Lambda}_0]_{ii} \geq [\mathbf{J}^{-1}]_{ii} \quad i \in \{1, 2\} \quad (27)$$

where  $\mathbf{J}$  is the  $2 \times 2$  Fisher's information matrix,



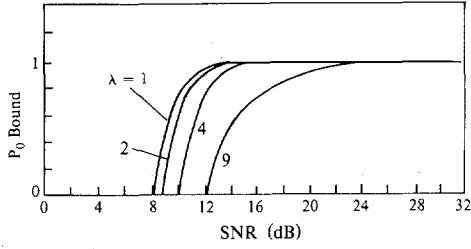


Fig. 14. Lower bound on  $p_0$  versus measurement SNR in the presence of shape modeling error.

$$[J]_{ik} = -\frac{2}{N_o} \left[ \frac{\partial^2 a(\boldsymbol{\epsilon})}{\partial \epsilon_i \partial \epsilon_k} \right]_{\boldsymbol{\epsilon}=\mathbf{0}} \triangleq -\frac{2}{N_o} \beta_{ik} \quad i, k \in \{1, 2\} \quad (28)$$

where  $a(\boldsymbol{\epsilon})$  is the ambiguity function in (I.23). One derivation of this expression comes from examining the error covariance for a linearized version of the problem (linearized about the actual object location); the ensuing linearized analysis holds for both perfect and imperfect modeling. In the latter case, the local error analysis corresponds to determining the estimate error covariance for a linear estimation problem in which the measurement model used is inaccurate.

For the case being considered in this section, the modeled object is the disk object in (2), the actual object is a constant-density object on an ellipse as shown in (20), and for simplicity, further assume that  $R = Ra$  and  $d = da$ . When the measurement aperture function  $h(t)$  is  $2W$  times the sinc function in (I.5),  $\beta_{ik}$  in (28) is given by

$$\beta_{ik} = \frac{4\pi E_a}{R^2 E_o(\lambda)} \mu_{\lambda}^{ik}(RW) \quad (29)$$

where

$$\begin{aligned} \mu_{\lambda}^{ik}(RW) = & \int_0^{\pi} \frac{\nu(\psi) d\psi}{\left( \lambda \cos^2 \psi + \frac{1}{\lambda} \sin^2 \psi \right)^{1/2}} \\ & \cdot \int_0^{2\pi RW} J_1 \left\{ \rho \left( \lambda \cos^2 \psi + \frac{1}{\lambda} \sin^2 \psi \right)^{1/2} \right\} \\ & \cdot J_1(\rho) d\rho \end{aligned} \quad (30)$$

where  $\nu(\psi)$  and  $E_a$  are given in (1.63) and (22), respectively.

For purposes of illustration, this expression has been evaluated for values of actual object eccentricity equal to 1, 2, 4, and 9, and the radius-bandwidth product  $RW$  equal to unity; the results are listed in Table I. By the central symmetry of the problem,  $\beta_{ik}$  is zero for  $i \neq k$ . This implies that the Fisher's information matrix is diagonal, in which case it is sufficient to consider  $\sigma_{11}$  and  $\sigma_{22}$  the diagonal elements in the inverse Fisher's information matrix. From (27)-(29),

$$\sigma_{ii} = \frac{R}{\sqrt{E_a/N_o}} \left( \frac{E_o(\lambda)}{8\pi \mu_{\lambda}^{ii}(RW)} \right)^{1/2} \quad (31)$$

The value of the second term on the right-hand side is also indicated in Table I.

Equation (31) is an expression for the standard deviation of the local error in the object location estimate when shape

TABLE I  
VALUES OF THE EXPRESSIONS IN (30) AND (31) FOR ECCENTRICITIES OF 1, 2, 4, AND 9

	$\mu_{\lambda}^{ik}(1)$			$\frac{\sigma_{ii}}{R} \left( \frac{E_a}{N_o} \right)^{1/2}$	
	$i=k=1$	$i=k=2$	$i \neq k$	$i=k=1$	$i=k=2$
$\lambda=1$	1.29	1.29	0.0	0.72	0.72
$\lambda=2$	0.71	1.26	0.0	0.95	0.72
$\lambda=4$	0.27	0.92	0.0	1.49	0.81
$\lambda=9$	0.09	0.58	0.0	2.32	0.94

modeling errors have been made. In order to develop insight into the relationship between these two standard deviations and the likelihood that a location estimate is obtained which lies within the actual object boundary, (31) may be used, for a given SNR, to identify an *error ellipse*, that is, the set of estimate points lying inside an ellipse centered at the actual object location, with semiaxis lengths equal to the estimate error standard deviations  $\sigma_{11}$  and  $\sigma_{22}$ . Notice from (31) that the size of this ellipsoidal region shrinks with increasing SNR.

For fixed values of SNR,  $RW$ , and object eccentricity  $\lambda$ , this error ellipse may be calculated and compared to the actual ellipsoidal object boundary. Fig. 15 illustrates the error ellipse specified in (31) for two representative eccentricities, namely  $\lambda = 2$  and 9, with a radius-bandwidth product of unity, and an SNR of 10 dB. As indicated by this figure, the 10 dB error ellipse is completely contained within the boundary of the actual ellipsoidal object (this is also true when the eccentricity equals 1 and 4). The results of this analysis provide insight into the effect of shape modeling errors on the local estimate error. For example, with  $\lambda$  equal to 9 (the actual object is highly eccentric but the modeled object is circularly symmetric), when the SNR is high enough for good global performance (say 20 dB, see Fig. 14), the location estimate is seen to be very likely to lie within the actual object boundary.

The information obtained from this analysis is valuable in identifying the maximum eccentricity of an object that can be located reliably when using a simple circularly symmetric modeled shape. In practice, if it is likely that the actual object eccentricity exceeds this value, a procedure that explicitly accounts for object eccentricity (see, for example, [14]) may be necessary in order to obtain an accurate location estimate.

#### IV. ROBUSTNESS TO THE PRESENCE OF UNMODELED OBJECTS

In this section, the degradation in localization performance is examined when, in addition to the object being located, one or more unmodeled objects exist within the cross section. Suppose that the actual field, shown in (3), consists of  $N$  disk objects, where the  $k$ th object has contrast  $d_k$ , location  $\mathbf{c}_k$ , and radius  $R_k$ . The object being located is denoted as the first ( $k = 1$ ) object, and  $k = 2, \dots, N$  correspond to unmodeled objects. From (8), the log likelihood function is given by

$$\begin{aligned} L(\mathbf{c}) = & \sum_{k=1}^N d_k \int_0^{\pi} \int_{-\infty}^{\infty} g(t - \mathbf{c}'_k \boldsymbol{\theta}, \theta; R_k) \\ & \cdot g_o(t - \mathbf{c}' \boldsymbol{\theta}, \theta; R) dt d\theta + n(\mathbf{c}, d, R). \end{aligned} \quad (32)$$

Letting  $E_o$  denote the energy in a unit-contrast, unit-radius

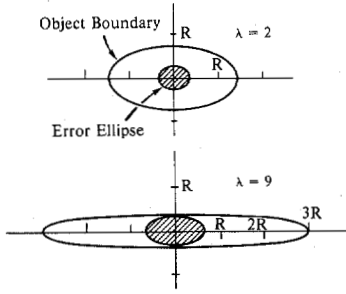


Fig. 15. Comparison of 10 dB localization error ellipse and object boundary in the presence of shape modeling error.

disk object [see (I.52)],  $E_k$ , the Radon-space energy in the  $k$ th object is given by

$$E_k = d_k^2 R_k^3 E_0. \quad (33)$$

The log likelihood function in (32) may be written as

$$L(\mathbf{c}) = \sum_{k=1}^N E_k \left( \frac{d}{d_a} \right) a^* \left( \frac{1}{R} (\mathbf{c} - \mathbf{c}_k), R/R_k \right) + n(\mathbf{c}, d, R) \quad (34)$$

where

$$a^* \left( \frac{1}{R} \boldsymbol{\epsilon}, R/R_k \right) = \frac{1}{E_0} \left( \frac{R}{R_k} \right)^2 \int_0^\pi \int_{-\infty}^{\infty} g \left( \frac{R}{R_k} t, \theta; 1 \right) \cdot g_0 \left( t - \frac{1}{R} \boldsymbol{\epsilon}' \boldsymbol{\theta}, \theta; 1 \right) dt d\theta. \quad (35)$$

This expression resembles that in (16), and in fact the normalized ambiguity function for the  $k$ th object in (35) may be obtained from Fig. 12 by replacing  $R/R_a$  with  $R/R_k$ .

In order to determine how the global performance is affected by the presence of unmodeled objects in the cross section, the vector of log likelihood means  $\mathbf{m}$  and the variance  $\sigma^2$  are determined and used in (10) to obtain a bound on  $p_0$ . The mean value of the log likelihood function at the point  $\boldsymbol{\gamma}_j$ , obtained from (34), is

$$m_j = E \{ L_j \} = \sum_{k=1}^N E_k \left( \frac{d}{d_k} \right) a^* \left( \frac{1}{R} (\boldsymbol{\gamma}_j - \mathbf{c}_k), R/R_k \right). \quad (36)$$

The variance of  $L_j$  is  $EN_0/2$ , as previously, where  $E$  is the energy in the modeled disk object  $E = d^2 R^3 E_0$ . A bound on  $p_0$  is given in (10), where

$$\begin{aligned} \frac{m_j}{\sigma} &= \left( \frac{2}{N_0 E} \right)^{1/2} \sum_{k=1}^N E_k \left( \frac{d}{d_k} \right) a^* \left( \frac{1}{R} (\boldsymbol{\gamma}_j - \mathbf{c}_k), R/R_k \right) \\ &= \left( \frac{2E_1}{N_0} \right)^{1/2} \left[ \left( \frac{R}{R_1} \right)^{-3/2} a^* \left( \frac{1}{R} (\boldsymbol{\gamma}_j - \mathbf{c}_1), R/R_1 \right) \right. \\ &\quad \left. + \left( \frac{R}{R_1} \right)^{3/2} \sum_{k=2}^N \left( \frac{R}{R_k} \right)^{-3} \left( \frac{d_k}{d_1} \right) \right. \\ &\quad \left. \cdot a^* \left( \frac{1}{R} (\boldsymbol{\gamma}_j - \mathbf{c}_k), R/R_k \right) \right]. \quad (37) \end{aligned}$$

Two specific examples are now investigated, the first involving a single unmodeled object, and the second involving the presence of numerous small objects distributed throughout the cross section. The latter case leads to random fluctuations in the background field, and may be thought of as corresponding to background field modeling errors.

*Example 2—A Single Unmodeled Object:* In this example, the degradation in global performance is investigated when the actual field consists of two objects, the first a disk object of size  $R_1 = R = T/10$ , contrast  $d_1 = d$  (perfectly matched to the model) situated at the point  $\mathbf{c}_a$ , and the second a disk object of unknown size  $R_U$  and contrast  $d_U$ , situated at the coordinates  $(6R, 0)$ . In this example the lower bound on  $p_0$  is examined, and its dependence on the measurement SNR and unmodeled object size and contrast is investigated.

Fig. 16 illustrates the lower bound on  $p_0$  [obtained using (10) and (37)] versus the contrast ratio  $d_U/d$  for several values of size ratio  $R/R_U$ , when the value of  $E_1/N_0$  equals 20 dB (i.e.,  $E_1/N_0 = 100$ ). This figure illustrates the graceful manner in which global performance degrades when a single unmodeled object is present in the cross section. Namely, when the unmodeled object is smaller than the modeled object ( $R/R_U = \frac{5}{3}$  and  $\frac{4}{3}$  curves), even if its contrast is equal to the value of the actual object contrast, global performance is virtually unaffected. Notice in particular the case of a smaller unmodeled object with a radius of 0.6 times the actual object radius—the unmodeled object can be *far* denser than the actual object without significant degradation in the ability to locate the main object by using an algorithm that does not take into account the possibility of more than one object.

*Example 3—Several Unmodeled Objects:* In this example, the global performance is investigated when numerous small unmodeled objects are distributed throughout the cross section. As mentioned, this may be thought of in a sense as corresponding to modeling errors in the background field, which, in all of our models for object estimation, has been assumed to be known perfectly. The actual field considered in this problem consists of the superposition of a disk object of radius  $R_1 = R = T/10$  and contrast  $d_1 = d$  (perfectly matched to the model) situated at the point  $\mathbf{c}_a$ , plus twenty smaller unmodeled disk objects each having unknown size  $R_u$  and contrast  $d_u$ , and located at various points on the rectangular lattice in (9). Fig. 17 illustrates the distribution of objects within the cross section when the size ratio  $R/R_u = 2$ , i.e., when each of the unmodeled objects has a radius half that of the actual object, which is located at the center of the disk  $C$ .

Fig. 18 illustrates the lower bound on  $p_0$  versus the contrast ratio  $d_u/d$  when  $E_1/N_0$  equals 20 dB, and the size ratio  $R/R_u$  equals 2 and  $\frac{4}{3}$  (that is, each of the unmodeled objects has a radius of 0.5 times the actual object radius in the first case, and a radius of 0.75 times the actual object radius in the second case). As indicated by this figure, the global localization performance is extraordinarily robust to the presence of smaller unmodeled objects, even when there are many of them. In particular, when the unmodeled object size is half the actual object size, the global performance is unaffected for values of unmodeled object contrast up to *twice* that of the actual object. Even when the unmodeled object radius is 0.75

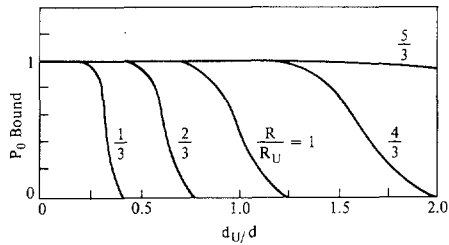


Fig. 16. Lower bound on  $p_0$  in the presence of an unmodeled object with contrast ratio  $d_u/d$ .

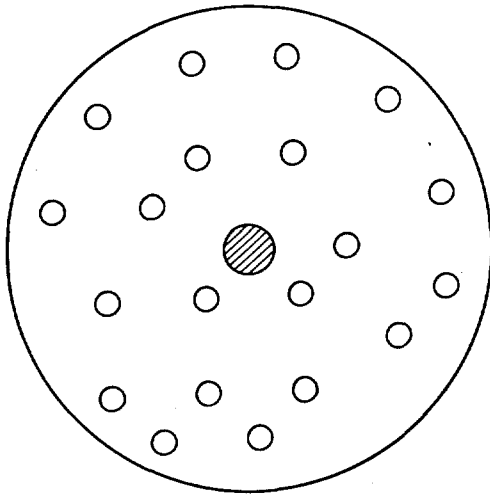


Fig. 17. Distribution of unmodeled objects in the cross section.

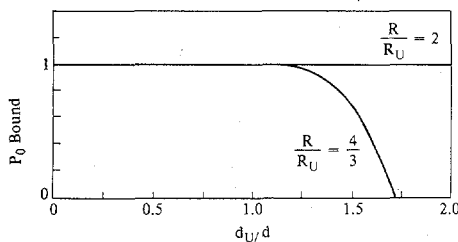


Fig. 18. Lower bound on  $p_0$  in the presence of 20 unmodeled objects with contrast ratio  $d_u/d$ .

times the actual object radius, the global performance is unaffected for unmodeled object contrast values less than or equal to the actual object contrast. The results of this robustness analysis suggest that the ML object localization procedure, which was developed assuming that the background field  $f_b(\mathbf{x})$  is known, is quite robust to random fluctuations in the background field about its assumed nominal distribution.

## V. CONCLUSIONS

In Part II, the way in which the single object localization performance is affected when the modeling assumptions in (1) do not hold was examined. In particular, the behavior of  $p_0$  was investigated in the presence of size and shape modeling errors, as well as in the presence of unmodeled objects within the cross section. Also, the Cramer-Rao bound was evaluated in the analysis of robustness to shape modeling errors in Section III.

The results of this analysis indicate that the ML localization

procedure developed in Part I is quite robust to a variety of modeling errors. In Section II, it was demonstrated that no major degradation in global performance occurs when the object size is in error by up to 50 percent of the actual object size. In Section III, it was shown that when the actual object shape differs from the modeled shape, the local and global localization performance is again quite insensitive to modeling errors. Finally, it was shown in Section IV that global performance is not affected significantly by the presence of unmodeled objects (even if there are many of them) that are smaller than approximately 0.75 the size of the object being located.

## APPENDIX A

### RADON SPACE SAMPLING FUNCTION $\xi_\Delta(t, \theta)$

*Proof of Claim 1:* From (21) and (23), the continuous-view ambiguity function is

$$\begin{aligned} a_\Delta(\boldsymbol{\epsilon}) &= \int_{\pi/2-\Delta}^{\pi/2+\Delta} \int_{-\infty}^{\infty} s(t, \theta) s(t - \boldsymbol{\epsilon}'\boldsymbol{\theta}, \theta) dt d\theta \\ &= \int_0^\pi \text{rect}\left[\frac{\pi - 2\theta}{4\Delta}\right] \int_{-\infty}^{\infty} s(t, \theta) s(t - \boldsymbol{\epsilon}'\boldsymbol{\theta}, \theta) dt d\theta \\ &= \mathbf{B} \left( \text{rect}\left[\frac{\pi - 2\theta}{4\Delta}\right] \cdot (s * \tilde{s}) \right) \end{aligned}$$

where  $\tilde{s}(t, \theta) \triangleq s(-t, \theta)$  and  $\mathbf{B}$  is the back-projection operator defined in (20).

$$\begin{aligned} a_\Delta(\boldsymbol{\epsilon}) &= \mathbf{B} \left( s * \int_{-\infty}^{\infty} \tilde{s}(\tau, \theta) \delta(t - \tau) \text{rect}\left[\frac{\pi - 2\theta}{4\Delta}\right] d\tau \right) \\ &= \mathbf{B} \left( s * \int_{-\infty}^{\infty} \tilde{s}(\tau, \theta) \xi_\Delta(t - \tau, \theta) d\tau \right) = \mathbf{B}(s * \tilde{s} * \xi_\Delta) \end{aligned}$$

(A1)

which agrees with (36), since  $s = \mathbf{R}f * h$  by (4).

### Back-Projection of $\xi_\Delta(t, \theta)$ <sup>4</sup>

From the definition of the back-projection operator in (20), the back-projection of the truncated impulse sheet  $\xi_\Delta(t, \theta)$  in (37) is given by

$$\begin{aligned} b_{\xi, \Delta}(\mathbf{x}) &= \int_0^\pi \xi_\Delta(\mathbf{x}'\boldsymbol{\theta}, \theta) d\theta = \int_0^\pi \delta(\mathbf{x}'\boldsymbol{\theta}) \text{rect}\left[\frac{\pi - 2\theta}{4\Delta}\right] d\theta \\ &= \int_{\pi/2-\Delta}^{\pi/2+\Delta} \delta(\mathbf{x}'\boldsymbol{\theta}) d\theta = \int_{\pi/2-\Delta}^{\pi/2+\Delta} \delta(r \cos(\theta - \phi)) d\theta \end{aligned}$$

(A2)

where  $(r, \phi)$  are the polar coordinates of  $\mathbf{x}$ ,  $r \in (-\infty, \infty)$ , and  $\phi \in [-\pi/2, \pi/2]$ . By a change of variable

<sup>4</sup>For an alternative derivation of the limited-view impulse response function, see Tuy [20].

$$b_{\xi, \Delta}(\mathbf{x}) = \int_{r \cos(\pi/2 - \theta - \Delta)}^{r \cos(\pi/2 - \phi + \Delta)} \frac{\delta(\tau) d\tau}{\sqrt{r^2 - \tau^2}} \quad (\text{A3})$$

which provides

$$b_{\xi, \Delta}(\mathbf{x}) = \begin{cases} \frac{1}{\|\mathbf{x}\|} & \text{if } |\phi| \leq \Delta \\ 0 & \text{otherwise.} \end{cases} \quad (\text{A4})$$

Fourier Transform of  $b_{\xi, \Delta}(\mathbf{x})$

The 2D Fourier transform of  $b_{\xi, \Delta}(\mathbf{x})$  in (A4) is given in terms of the polar coordinates  $(r, \phi)$  as

$$B_{\xi, \Delta}(\boldsymbol{\omega}) = \int_{-\Delta}^{\Delta} \int_{-\infty}^{\infty} \frac{1}{|r|} e^{-j2\pi r(\omega_1 \cos\phi + \omega_2 \sin\phi)} |r| dr d\phi \\ = \int_{-\Delta}^{\Delta} d\phi \int_{-\infty}^{\infty} e^{-j2\pi r \boldsymbol{\omega}' \boldsymbol{\phi}} dr \quad (\text{A5})$$

where  $\boldsymbol{\phi} = (\cos\phi \sin\phi)'$  and  $\boldsymbol{\omega} = (\omega_1 \omega_2)'$ .

The second integral in (A5) is the 1D Fourier transform, evaluated at  $\boldsymbol{\omega}'\boldsymbol{\phi}$ , of a function that is unity for all  $r$ . Thus,

$$B_{\xi, \Delta}(\boldsymbol{\omega}) = \int_{-\Delta}^{\Delta} \delta(\boldsymbol{\omega}'\boldsymbol{\phi}) d\phi. \quad (\text{A6})$$

Equation (A6) has the same form as (A2), and by a change of variable yields

$$B_{\xi, \Delta}(\boldsymbol{\omega}) = \begin{cases} \frac{1}{\|\boldsymbol{\omega}\|} & \text{if } \left| \psi - \frac{\pi}{2} \right| \leq \Delta \\ 0 & \text{otherwise} \end{cases} \quad (\text{A7})$$

where  $\psi$  is the angular polar coordinate of the point  $\boldsymbol{\omega}$ .

APPENDIX B

CALCULATING  $A(\boldsymbol{\omega})$

In terms of the Radon transform and back-projection operators  $R$  and  $B$  in (1) and (20), CBP with a  $\theta$ -dependent convolving kernel  $z(t, \theta)$  may be written as

$$\hat{f}(\mathbf{x}) = \int_0^\pi \int_{-\infty}^{\infty} g(t, \theta) z(t - \mathbf{x}'\boldsymbol{\theta}, \theta) dt d\theta = B(Rf * \tilde{z}) \quad (\text{B1})$$

where  $\tilde{z}(t, \theta) \triangleq z(-t, \theta)$ , and  $*$  denotes 1D convolution in  $t$ ,

$$[z_1 * z_2](\tau) = \int_{-\infty}^{\infty} z_1(t, \theta) z_2(\tau - t, \theta) dt. \quad (\text{B2})$$

Letting  $**$  denote 2D convolution, it is shown in Davison and Grunbaum [19] that (B1) may be rewritten as

$$B(Rf * \tilde{z}) = f ** B(\tilde{z}), \quad (\text{B3})$$

that is, CBP operating on  $Rf$  with a convolving kernel  $z(t, \theta)$  may be written as the 2D convolution of  $f(\mathbf{x})$  with the back-projection of  $\tilde{z}(t, \theta)$ .

The relationship in (B3) leads to an expression for the Fourier transform of the ambiguity function. In particular, from (36),

$$a(\boldsymbol{\epsilon}) = B(Rf * h * R\tilde{f} * h * \xi). \quad (\text{B4})$$

Here,  $f(\mathbf{x}) = d \cdot f_o(\mathbf{x})$  is the object situated at the origin and having contrast  $d$ ,  $f(x_1, x_2) \triangleq f(-x_1, -x_2)$ , and  $\xi$  is the sampling function given in (37). Denoting by  $r_h(\mathbf{x})$  the circularly symmetric 2D function satisfying  $R(r_h(\mathbf{x})) = h(t)$  (that is, a central slice of  $R_h(\boldsymbol{\omega})$ , the 2D Fourier transform of  $r_h(\mathbf{x})$ , is given by  $H(\boldsymbol{\omega})$ , the 1D Fourier transform of  $h(t)$ ), and successively applying (B3),

$$a(\boldsymbol{\epsilon}) = f ** r_h ** \tilde{f} ** r_h ** b_{\xi}. \quad (\text{B5})$$

Taking 2D Fourier transforms, and noting that  $f$  is real,

$$A(\boldsymbol{\omega}) = |F(\boldsymbol{\omega})|^2 R_h^2(\boldsymbol{\omega}) B_{\xi}(\boldsymbol{\omega}). \quad (\text{B6})$$

APPENDIX C

LOG LIKELIHOOD FUNCTION  
PROBABILITY BOUND

Let  $L$  denote the  $M$ -vector of log likelihood function values at the points  $\gamma_j, j = 1, 2, \dots, M$ , which is a Gaussian random vector having mean  $m$  and covariance  $\sigma^2 I$ . As in Part I, let  $p_j$  denote the probability of  $E_j$ , the event that the maximum log likelihood function value occurs at the point  $\gamma_j$ . The log likelihood function noise depends only on the modeled, and not the actual, object parameters; as was done in Part I, the normalized ambiguity function for the modeled object (i.e.,  $E\{n^2(\mathbf{c}, d, R)\}$ ) is approximated as being equal to zero at distances exceeding  $2R$ . Under this approximation, the elements in  $L$  are uncorrelated, and  $(1 - p_j)$  may be bounded using the approach in [13, p. 264],

$$1 - p_j = \text{Prob} \{ \text{any } L_i > L_j, i \neq j \} \\ = \text{Prob} \{ L_1 > L_j \text{ or } L_2 > L_j \text{ or } \dots \text{ or } L_M > L_j \} \\ \leq \text{Prob} \{ L_1 > L_j \} + \text{Prob} \{ L_2 > L_j \} + \dots \\ + \text{Prob} \{ L_M > L_j \} \\ = \sum_{i \neq j} \int_{-\infty}^{\infty} dL_j p(L_j) \int_{L_j}^{\infty} p(L_i) dL_i. \quad (\text{C1})$$

Substituting the Gaussian distribution and simplifying,

$$p_j \geq 1 - \sum_{i \neq j} \int_{-\infty}^{\infty} \frac{1}{\sqrt{2\pi}} \exp \left\{ -\frac{1}{2}(x_j - \Delta_{ij})^2 \right\} \\ \cdot dx_j \int_{x_j}^{\infty} \frac{1}{\sqrt{2\pi}} \exp \left( -\frac{x_i^2}{2} \right) dx_i \quad (\text{C2})$$

where

$$\Delta_{ij} \triangleq \frac{1}{\sigma} (m_j - m_i). \quad (\text{C3})$$

By a change of variable corresponding to a 45° coordinate system rotation, (C2) may be written as

$$p_j \geq 1 - \sum_{i \neq j} \int_{\Delta_{ij}/\sqrt{2}}^{\infty} \frac{1}{\sqrt{2\pi}} \exp\left(-\frac{x^2}{2}\right) dx. \quad (C4)$$

## REFERENCES

- [1] L. A. Shepp and B. F. Logan, "The Fourier reconstruction of a head section," *IEEE Trans. Nucl. Sci.*, vol. NS-21, pp. 21-43, 1974.
- [2] R. M. Mersereau and A. V. Oppenheim, "Digital reconstruction of multidimensional signals from their projections," *Proc. IEEE*, vol. 62, pp. 1319-1338, 1974.
- [3] S. W. Rowland, "Computer implementation of image reconstruction formulas," in *Image Reconstruction from Projections—Implementation and Applications* (Topics in Applied Physics, vol. 32), G. T. Herman, Ed. New York: Springer-Verlag, 1979.
- [4] V. V. Klyuev, E. I. Vainberg, I. A. Kazek, and V. P. Kurozaev, "Computational tomography—A new radiation method of non-destructive testing, I, II," *Sov. J. Nondestruct. Test.*, vol. 16, pp. 180-185, 186-193, 1980.
- [5] W. Munk and C. Wunsch, "Ocean acoustic tomography: A scheme for large scale monitoring," *Deep Sea Res.*, vol. 26A, pp. 123-161, 1979.
- [6] K. M. Hanson, "Detectability in the presence of computed tomographic reconstruction noise," *Proc. SPIE*, vol. 127, Medicine VI, pp. 304-312, 1978.
- [7] P. G. Selfridge and J. M. S. Prewitt, "Organ detection in abdominal computerized tomography scans: Application to the kidney," *Comput. Graphics Image Processing*, vol. 15, pp. 265-278, 1981.
- [8] G. H. Glover and N. J. Pelc, "An algorithm for the reduction of metal clip artifacts in CT reconstructions," *Med. Phys.*, vol. 8, pp. 799-807, 1981.
- [9] B. Cornuelle, "Acoustic tomography," *IEEE Trans. Geosci. Remote Sensing*, vol. GE-20, pp. 326-332, 1982.
- [10] K. A. Dines and R. J. Lytle, "Computerized geophysical tomography," *Proc. IEEE*, vol. 67, pp. 1065-1073, 1979.
- [11] R. L. Parker, "Understanding inverse theory," *Ann. Rev. Earth Planet. Sci.*, vol. 5, pp. 35-64, 1977.
- [12] R. Gordon, "Artifacts in reconstructions made from a few projections," in *Proc. First Int. Joint Conf. Pattern Recog.*, pp. 275-285, 1973.
- [13] H. L. Van Trees, *Detection, Estimation, and Modulation Theory, Part I, Detection, Estimation, and Linear Modulation Theory*. New York: Wiley, 1968.
- [14] D. Rossi, "Reconstruction from projections based on detection and estimation of objects," Ph.D. dissertation, Dep. Elec. Eng. Comput. Sci., Massachusetts Inst. Technol., Cambridge, 1982.
- [15] R. Bracewell, *The Fourier Transform and Its Applications*. New York: McGraw-Hill, 1965.
- [16] S. J. Riederer, N. J. Pelc, and D. A. Chesler, "The noise power spectrum in computed X-ray tomography," *Phys. Med. Biol.*, vol. 23, pp. 446-454, 1978.
- [17] H. L. Van Trees, *Detection, Estimation, and Modulation Theory, Part III, Radar-Sonar Signal Processing and Gaussian Signals in Noise*. New York: Wiley, 1971.
- [18] R. G. Gallager and C. W. Helstrom, "A bound on the probability that a Gaussian process exceeds a given function," *IEEE Trans. Inform. Theory*, vol. IT-15, pp. 163-166, 1969.
- [19] M. E. Davison and F. A. Grunbaum, "Tomographic reconstruction with arbitrary directions," *Commun. Pure Appl. Math.*, vol. 34, pp. 77-120, 1981.
- [20] H. Tuy, "Reconstruction of a 3-dimensional object from a

limited range of views," *J. Math. Analysis Appl.*, vol. 80, pp. 598-616, 1981.

- [21] M. I. Skolnik, *Introduction to Radar Systems*. New York: McGraw-Hill, 1962.



David J. Rossi (S'74-M'82) was born in Binghamton, NY, in 1953. He received both the B.S. degree in biomedical engineering and the M.Eng. degree in electrical engineering from Rensselaer Polytechnic Institute, Troy, NY, in 1976 and 1977, respectively, and the Ph.D. degree in electrical engineering from Massachusetts Institute of Technology, Cambridge, in 1982.

From 1977 to 1978 he held a Schlumberger Foundation Fellowship, from 1979 to 1980 he held a Vinton Hayes Fellowship, and from 1980 to 1982 he was a Research Assistant with the Laboratory for Information and Decision Systems at M.I.T., doing research in the area of reconstruction of objects from projections. He is currently with Schlumberger-Doll Research, Ridgefield, CT, where he is active in the area of resistivity well logging and stochastic modeling, estimation, and detection.

Dr. Rossi is a member of Tau Beta Pi and the Sigma Xi Research Society.



Alan S. Willsky (S'70-M'73-SM'82) received both the S.B. degree and the Ph.D. degree from the Massachusetts Institute of Technology, Cambridge, in 1969 and 1973, respectively. From 1969 through 1973 he held a Fannie and John Hertz Foundation Fellowship.

He joined the M.I.T. faculty in 1973 and his present position is Professor of Electrical Engineering. From 1974 to 1981 he served as Assistant Director of the M.I.T. Laboratory for Information and Decision Systems. He is also a founder and member of the Board of Directors of Alphatech, Inc. In 1975 he received the Donald P. Eckman Award from the American Automatic Control Council. He has held visiting positions at Imperial College, London, England, and L'Université de Paris-Sud, Paris, France. His present research interests are in problems involving abrupt changes in signals and systems, multidimensional estimation, decision-directed signal processing, and the asymptotic analysis of control and estimation systems.

Dr. Willsky is Editor of the M.I.T. Press series on signal processing, optimization, and control, was Program Chairman for the 17th IEEE Conference on Decision and Control, is an Associate Editor of several journals including the IEEE TRANSACTIONS ON AUTOMATIC CONTROL, is a member of the Board of Governors of the IEEE Control Systems Society, and was Program Chairman for the 1981 Bilateral Seminar on Control Systems held in the People's Republic of China. He also gave the opening plenary lecture at the 20th IEEE Conference on Decision and Control. He is the author of the research monograph *Digital Signal Processing and Control and Estimation Theory* and is co-author of the undergraduate text *Signals and Systems*. He was awarded the 1979 ASCE Alfred Noble Prize and the 1980 IEEE Browder J. Thompson Memorial Prize Award for a paper excerpted from his monograph.